Interplay between abiotic and biotic processes for travertine formation from thermal springs

Stefania Venturi[a,b], Simona Crognale[c], Francesco Di Benedetto[d,*], Giordano Montegrossi[b], Barbara Casentini[c], Stefano Amalfitano[c], Tommaso Baroni[a], Simona Rossetti[c], Franco Tassi[a,b], Francesco Capecchiacci[a,b,e], Orlando Vaselli[a,b], Stefano Fazi[c,*]

[a]*Department of Earth Sciences, University of Florence, Via G. La Pira 4, 50121 Firenze (Italy)*

[b]*Institute of Geosciences and Earth Resources (IGG), National Research Council of Italy (CNR), Via G. La Pira 4, 50121 Firenze (Italy)*

[c]*Water Research Institute (IRSA), National Research Council of Italy (CNR), Via Salaria km 29.300, 00015 Monterotondo, Rome (Italy)*

[d]*Department of Physics and Earth Sciences, University of Ferrara, Via Saragat 1, 44122 Ferrara (Italy)*

[e]*Istituto Nazionale di Geofisica e Vulcanologia, Sezione di Napoli, Osservatorio Vesuviano, via Diocleziano, 328 80124 Napoli (Italy)*

* Corresponding authors. E-mail: francesco.dibenedetto@unife.it, stefano.fazi@irsa.cnr.it

Submitted to Geobiology

Abstract

Active hydrothermal travertine systems are ideal environments to investigate how abiotic and biotic processes affect mineralization mechanisms and the mineral fabric formation. In this study, a biogeochemical characterization of waters, dissolved gases and microbial mats was performed together with a mineralogical investigation on travertine encrustations at Piscine Carletti (*PC*) spring system (Viterbo thermal area, Latium, Italy). The comprehensive model, compiled by means of TOUGHREACT computational tool from measured parameters, revealed that the overall physicochemical environmental conditions were not able to explain the presence of mineralogical phases or fabrics which were largely influenced by microenvironmental conditions induced by microbial mats. The latter consisted of well-structured microbial communities largely shaped by light availability and temperature conditions, which varied along the *PC* system. Nevertheless, mineralogical features were homogeneous throughout the system with euhedral calcite crystals, related to inorganic precipitation induced by CO_2 degassing, coexisting with calcite shrubs associated with organomineralization processes, indicating an indirect microbial participation in the deposition process. Similarly, microbial activity played a role in driving calcite redissolution processes, resulting in circular pits on calcite crystal surfaces possibly related to the metabolic activity of S-oxidizing bacteria occurring in the microbial mats. The latter might also explain the apparent contradiction between the undersaturated conditions with respect to gypsum based on measured physicochemical parameters and the recognition of gypsum crystals embedded in microbial mats. Gypsum precipitation was likely induced by supersaturated microenvironmental conditions determined by local increase in sulfate concentration, likely produced by S-oxidizing bacteria. Moreover, the absence of dissolution on gypsum crystals despite the overall undersaturated environmental conditions suggested the capability of microbial mats in modulating environmental mobility of chemical species by providing a protective barrier on gypsum crystals.

***Keywords**: microbial mat, biofilm-mediated mineralization, gypsum, travertine, hot spring*

Graphical abstract:

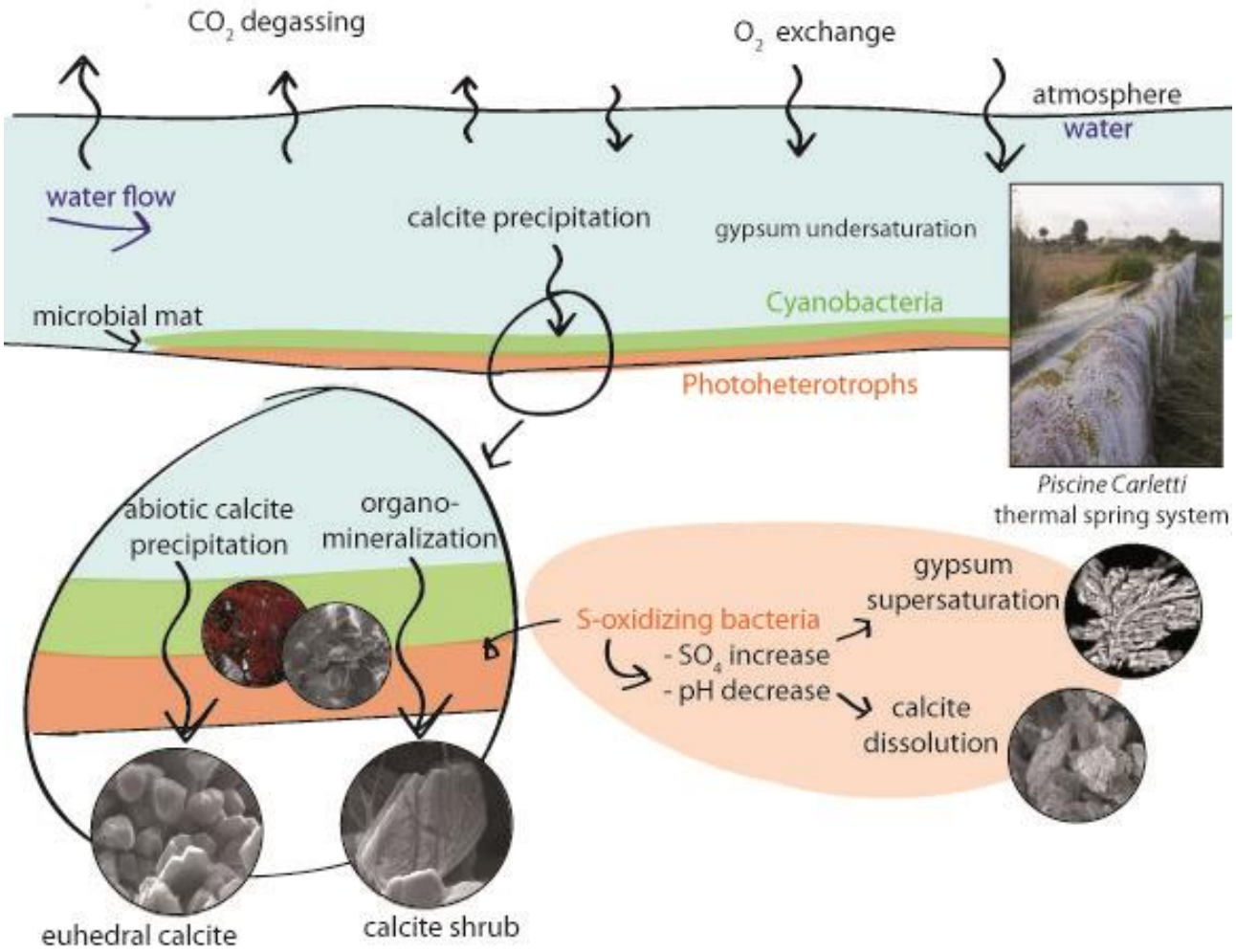

1. Introduction

Terrestrial hot springs typically harbor rich and diverse microbial communities able to thrive in extreme environmental conditions through peculiar adaptation strategies, including the formation of heterogeneous syntrophic assemblages and microbial mats, adhesion to solid surfaces and mineral deposits, establishment of complex biotic and abiotic interactions with the surrounding highly dynamic geochemical environment (Schuler et al., 2017 ; Des Marais and Walter, 2019).

Microbial mats are vertically structured microbial communities that significantly affect mineral precipitation and dissolution processes occurring at the water-solid interface (e.g. van Gemerden, 1993; Prieto-Barajas et al., 2018). Depending on the role of biological activity, microbe-mineral interactions may result in diverse mineral precipitation processes, as follows: (i) *biologically-controlled* mineralization, in which biotic processes directly govern the crystal nucleation and growth shaping mineral morphologies; (ii) *biologically-induced* mineralization, resulting from the interaction between metabolic byproducts and the chemical environment, and (iii) *biologically-influenced* mineralization (also referred to *organomineralization*), induced by abiotic processes but with the influence of active organisms on crystal morphology and composition (Dupraz et al., 2009; Castro-Alonso et al., 2019). In the latter case, mineral precipitation is favored by nucleation on bacterially-produced organic polymers (Görgen et al., 2020), such as those forming cell surfaces or extracellular polymeric substances (EPS). Similarly, microbial mats may induce or inhibit mineral dissolution as due to either a direct result of metabolic activity or metabolically-induced chemical gradients at the microscale level (Wilmeth et al., 2018).

Understanding geobiological processes and microbe-mineral interactions is of paramount relevance for both understanding the biogeochemical functioning of early life forms on Earth and correctly identifying biosignatures in either rock records or extra-terrestrial materials gathering paleobiological and paleoecological information (Allen et al., 2000; Banfield et al., 2004; Tang et al., 2014; Della Porta et al., 2021).

In this study, a biogeochemical investigation was performed at the *Piscine Carletti* (PC) spring system that belongs to the Viterbo geothermal area (Latium, Central Italy). PC has a long-lasting interest because of its peculiar configuration, enabling its use as an "open-air" laboratory. The thermal water is indeed discharged at approximately 60 °C (Piscopo et al., 2006) and conveyed into a 12×12 m^2 pool, through a 120 m long artificial channel, along which travertine deposition is occurring, allowing the establishment of a clear biogeochemical gradient. An extensive characterization of (i) water and dissolved gas chemistry, (ii) travertine encrustation at the bottom of the channel, and (iii) microbial

community structure in both the water and the solid phase at and below the solid-liquid interface was carried out along the whole channel. All experimental findings were compared with a comprehensive model carried out by means of the TOUGHREACT computational tool. The aims of the study were to (i) understand the mutual influence between biotic and abiotic components, (ii) unravel mineralization mechanisms during travertine formation, and (iii) characterize the biological impact of microbial mats on mineral fabric structuring.

2. Study area

Piscine Carletti (hereafter named *PC*; also referred as *Bullicame 3* or *Bullicame West*; Duchi et al., 1985; Pentecost, 1995; Minissale et al., 2002; Di Benedetto et al., 2011; Rimondi et al., 2021) is located in a thermal area sited between the Central Apennines and Tyrrhenian coastline, few km west of the town of Viterbo (northern Latium, Central Italy; **Fig. 1**). This region is characterized by (i) a Paleozoic-Triassic metamorphic basement, (ii) Mesozoic-Paleogene sedimentary rocks related to the Apennine orogenesis, and (iii) upper Mio-Pleistocene sedimentary basins related to a post-collisional extensional phase (Piscopo et al., 2006; Baiocchi et al., 2012) during which the Vicano-Cimino Volcanic District (VCVD) formed (Tassi et al., 2015). Crustal thinning, igneous processes and high heat flow in this area are responsible of the large number of CO_2(H_2S)-rich thermo-mineral springs and anomalously high CO_2 diffuse degassing sites (Cinti et al., 2014), whose location is strictly controlled by (i) hydrogeological settings and (ii) brittle structural elements (Minissale et al., 2004). The resulting complex geological setting has originated the occurrence of two main aquifers, as follows: (i) a shallower volcanic aquifer, characterized by cold and fresh waters with Ca-HCO_3 composition and low pCO_2 values, located within the Pleistocene volcanites, and (ii) a deeper aquifer, located in the deep Mesozoic-Cenozoic carbonate rocks, hosting thermal waters at 220 °C with a Ca-SO_4(HCO_3) composition and high pCO_2 values, mainly produced by thermometamorphic decarbonation processes and mantle degassing (Piscopo et al., 2006; Baiocchi et al., 2012; Cinti et

106 al., 2014). The Viterbo geothermal system is located in coincidence with a structural high of the
107 carbonate basement and a geothermal gradient greater than 100 °C/km (Piscopo et al., 2006), resulting
108 in CO_2- and H_2S-rich thermal waters uprising through faults and fractures, with temperatures ranging
109 around 50-60 °C (Duchi and Minissale, 1995; Minissale, 2004; Cinti et al., 2014).
110 At *PC*, the hot water emerges at a relatively constant flow rate (0.7 L/s; Di Benedetto et al., 2011) in
111 a constructed pool (ca. 3 m in diameter), where vigorous gas bubbling occurs. Then, it flows along a
112 narrow (14 cm) artificial channel, elevated with respect to the ground level (up to 2 m). The channel
113 ends into a pool where waters cool down to ambient temperature (**Fig. 1**). The artificial elements are
114 covered by a thick travertine deposit with shrub fabrics (Di Benedetto et al., 2011), partially coated
115 by differently colored biofilms and algae. The channel is periodically maintained to guarantee the
116 regular downstream water flow.

117

118 **3. Material and Methods**

119 **3.1 Sampling strategy**

120 Water, dissolved gas, biofilm and travertine sampling at *PC* was carried out in March 2016 in eight
121 selected sites along the artificial channel, at a distance of 14 m from each other, starting from the
122 farthest site with respect to the water spring and proceeding upstream (i.e. from C8 to C1; **Fig. 1**) to
123 avoid any sampling-induced contamination.

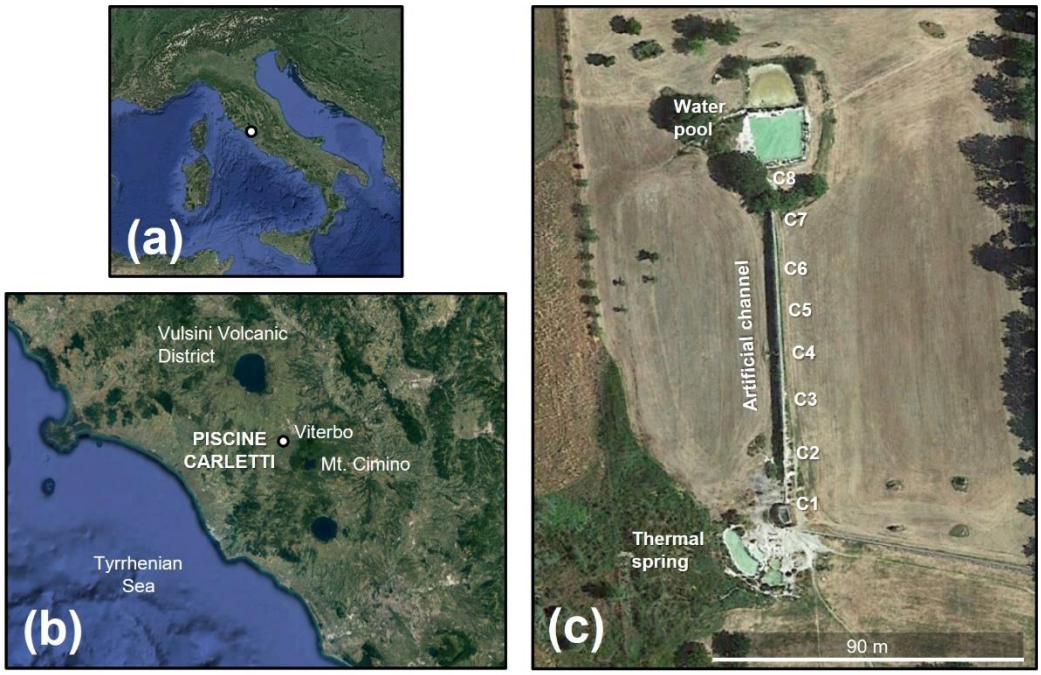

Figure 1 Location of the study area in central Italy (a), few km west of the town of Viterbo (b). The Piscine Carletti spring system is shown, together with the sampling sites along the channel (c).

3.2 Water and dissolved gas sampling and analysis

At each sampling site, pH, temperature (T, °C) and dissolved oxygen (DO, mg/L) were measured *in situ* with a Hach HQ 40d probe. Alkalinity was determined directly in the field via acidimetric titration with 0.01 N HCl and methyl-orange as indicator. Three filtered (0.45 µm) water aliquots were collected in polyethylene bottles at each site, as follows: (i) 125 mL aliquot for the analysis of main anions (SO_4^{2-}, Cl^-, F^-, NO_3^-, Br^-), (ii) 50 mL aliquot acidified with 0.5 mL of Suprapur HCl for the determination of the main cations (Ca^{2+}, Mg^{2+}, Na^+, K^+), (iii) 50 mL aliquot acidified with 0.5 mL of Suprapur HNO_3 for the analysis of trace elements. Moreover, an unfiltered water aliquot was sampled in 125 mL polyethylene bottles, where few milligrams of $HgCl_2$ were added in the laboratory in order to prevent any microbial activity, for the analysis of $^{13}C/^{12}C$ values of the total dissolved inorganic carbon (TDIC). Dissolved Organic Carbon (DOC) was sampled in HCl pre-conditioned PTFE 20 ml bottles, filtered on 25 mm carbon cleaned GF/F filters (combusted at 450°C for 4 h) and acidified

0.2% after sampling with Suprapur HCl. Samples were on site analyzed for NO_2^- and NH_4^+ content by portable spectrophotometer measurements (Hach DR 2800).

Dissolved gases were collected at each site using pre-evacuated 250 mL Pyrex flasks equipped with Thorion® valve and filled with water up to about 3/4 of their inner volume (Tassi et al., 2008, 2009). The chemical composition was calculated from the composition of the gas phase stored in the headspace of the sampling glass flasks on the basis of (i) gas pressure, (ii) headspace volume and (iii) the solubility coefficients of each gas compound (Tassi et al., 2018).

The main anions and cations were analyzed by ion chromatography (761 Compact IC- Methrom and 861 Advanced Compact IC-Metrohm, respectively). Trace elements (Mn, Fe, Co, Ni, Cu, Zn, Ba, and Sb) were determined by Inductively Coupled Plasma Optical Emission Spectrometry (ICP-OES) with PerkinElmer Optima 8200. The analytical errors for IC and ICP-OES were ≤5 and ≤10%, respectively. DOC samples were analyzed by Shimadzu TOC analyzer. NH_4^+ was spectrophotometrically detected at 420 nm, (3 drops Seignette salt and 0.3 mL Nessler reagent were added to 5 mL sample and measured after 3 min) . NO_2^- was diazotated and spectrophotometrically detected at 543 nm, (0.1 mL solfanilamide and 0.1 mL NEDA reagent was added to 5 mL sample and measured after 6 min).

The δ^{13}C-TDIC values (expressed as ‰ vs. V-PDB) were analyzed with a Finnigan Delta Plus XL mass spectrometer in CO_2 recovered after the reaction of 3 mL of water with 2 mL of anhydrous H_3PO_4 in pre-evacuated sample holders, which were then left in a thermostatic bath at 25 ± 0.1 °C for 12h. The CO_2 was extracted and purified by using a two-step cryogenic (liquid N_2 and a mixture of liquid N_2 trichloroethylene; Evans et al., 1988; Vaselli et al., 2006) procedure (Salata et al., 2000). The analytical error for δ^{13}C-TDIC values was ±0.05 ‰.

The chemical composition of the main inorganic compounds (CO_2, N_2, Ar, O_2 and He) stored in the headspace of the sampling flasks was analyzed using a Shimadzu 15A gas chromatograph (GC) equipped with a 9 m long molecular sieve column and Thermal Conductivity Detector (TCD). The analysis of CH_4 was carried out using a Shimadzu 14A gas chromatograph equipped with a Flame

Ionization Detector (FID) and a 10 m long stainless steel column packed with Chromosorb PAW 80/100 mesh coated with 23% SP 1700 (Vaselli et al., 2006; Tassi et al., 2008). The analytical error for GC analysis was ≤5%. The total amount of dissolved gases was then calculated according to the Henry's law.

The $^{13}C/^{12}C$ isotopic ratios of dissolved CO_2 (expressed as $\delta^{13}C\text{-}CO_2$ in ‰ vs. V-PDB) were determined on the basis of those measured on the gaseous CO_2 stored in the sampling flask headspace ($\delta^{13}C\text{-}CO_{2\_STRIP}$). The $\delta^{13}C\text{-}CO_{2\_STRIP}$ values were analyzed by a Finnigan Delta Plus XL mass spectrometer after a two-step extraction and purification procedure of the gas mixture, as described for the analysis of the $\delta^{13}C$-TDIC values. Internal (Carrara and San Vincenzo marbles) and international (NBS18 and NBS19) standards were used for the estimation of external precision. The analytical error and the reproducibility were ±0.05 ‰ and ±0.1 ‰. The $\delta^{13}C\text{-}CO_2$ values were then calculated from the measured $\delta^{13}C\text{-}CO_{2\_STRIP}$ (Venturi et al., 2017) based on the enrichment factor (ε_1) for gas-water isotope equilibrium proposed by Zhang et al. (1995), as follows:

$$\delta^{13}CO_2 = \varepsilon_1 + \delta^{13}CO_{2\_STRIP} = (0.0049 \times T(°C)) - 1.31 + \delta^{13}CO_{2\_STRIP}$$

3.3 Sampling and analysis for microbial community characterization of waters and biofilms

At each sampling site, 1 L of water was filtered through polycarbonate membranes (pore size 0.2 μm, 47 mm diameter, Nuclepore) and immediately stored at -20 °C for DNA extraction. Moreover, 100 mL of water for the microbial community characterization were fixed in formaldehyde solution (FA, 1% vol/vol final concentration) and kept at 4 °C until analyses (performed within 24h). Sub-aliquots (30-80 mL) were filtered on polycarbonate membrane filters (Nuclepore filters: 47 mm diameter with pore size of 0.2 μm) by gentle vacuum (<0.2 bar) and the preparations were washed with 20 mL of Milli-Q water. The obtained filters were stored at -20 °C until further processing.

Biofilm grown on travertine deposit along the channel bed under was collected at the same time as water sampling. In detail, fourteen biofilm samples were collected at the same sampling points of water samples from the superficial (2 cm depth) and sub-superficial layer of travertine deposit (8 cm

depth), with the sole exception of the first (C1) and last sampling (C8) points where only the superficial layer was collected. Core biofilm samples were obtained by drilling the travertine deposit using plastic cylinder with around 1 cm diameter in order to keep unaltered the biofilm structure and stratification. These core samples were immediately stored at -20 °C and successively used for DNA extraction. Furthermore, around 1 g of superficial and sub-superficial layer was collected by using a plastic spoon and immediately stored at +4 °C until analyses. In laboratory, these aliquots were diluted (1:10 w/v) with sterilized buffer solution containing formaldehyde in 15 mL Falcon tubes and further processed using Nycodenz density gradient centrifugation, as described elsewhere (Amalfitano and Fazi (2008). Then, the liquid suspensions were filtered on polycarbonate membrane filters and used for microscopy observation.

Total prokaryotic abundance was estimated by DAPI staining while those of Bacteria and Archaea were determined by Catalyzed Reported Deposition – Fluorescence in situ Hybridization (CARD-FISH), following the protocol optimized by Fazi et al. (2007, 2013) using specific rRNA-target HRP-labelled probes (Biomers, Ulm, Germany): EUB338 I-III for *Bacteria*; ALF968 for *Alphaproteobacteria*; BET42a for *Betaproteobacteria*; GAM42a for *Gammaproteobacteria*; DELTA495 for *Deltaproteobacteria*; CFX and GNSB for *Chloroflexi*, LGC354 for *Firmicutes*, CF319a for *Flavobacteria*, PLA46 for *Planctomycetes*, TM7905 for TM7, HGC69A for *Actinobacteria* and ARCH915 for *Archaea*. Details of probes are available at probeBase (Greuter et al., 2016). The stained filter sections were inspected on a Leica DM LB 30 epifluorescence microscope (Leica Microsystems GmbH, Wetzlar, Germany) at 1000× magnification. At least 300 cells were counted in >10 microscopic fields randomly selected across the filter sections. The relative abundance of hybridized cells was estimated as the ratio of hybridized cells to total DAPI-stained cells.

The abundance of microbial free-living cells and aggregates was determined by using the Flow Cytometer A50-micro (Apogee Flow System, Hertfordshire, England) equipped with a solid state laser set at 20 mV and tuned to an excitation wave length of 488 nm. The volumetric absolute cell

counting was carried out on samples stained with SYBR Green I (1:10,000 dilution; Molecular Probes, Invitrogen). Apogee Histogram Software (v89.0) was used to plot and analyze data; the light scattering signals (forward and side scatters) and the green fluorescence (530/30 nm) were considered for the single cell characterization. Thresholding was set on the green channel and voltages were adjusted to place the background and instrumental noise below the first decade of green fluorescence. Samples were run at low flow rates to keep the number of events below 1000 events s^{-1}. The intensity of green fluorescence emitted by SYBR-positive cells allowed for the discrimination among cell groups exhibiting two different nucleic acid content (cells with Low Nucleic Acid content - LNA; cells with High Nucleic Acid content - HNA) (Amalfitano et al., 2014).

Approximately 1g of biofilm sample was used for DNA extraction with PowerSoil® DNA Isolation Kit (MoBio - Carlsbad, CA) by following the manufacturer's instructions. For water samples, DNA was extracted utilizing one entire polycarbonate membrane for each sample. The quality of extracted DNA ($1.6 < A260/280 < 1.8$ and $A260/230 > 2$) was analyzed with a Nanodrop 3300 (Thermo Scientific, Italy). DNA was stored at − 20 °C in small aliquots.

Bacterial and archaeal V3-4 16S sequencing libraries were prepared by a custom protocol based on an Illumina protocol (Illumina, 2015). Up to 10 ng of extracted DNA was used as template for PCR amplification of the 16S gene fragments. Each PCR reaction (25 μL) contained dNTPs (100 μM of each), MgSO4 (1.5 mM), Platinum® Taq DNA polymerase HF (1 U), 1X Platinum® High Fidelity buffer (Thermo Fisher Scientific, USA) and tailed primermix (400 nM of each forward and reverse). PCR was run according to the following program: initial denaturation at 95 °C for 2 min, 35 cycles of amplification (95 °C for 20 s, 50 °C for 30 s, 72 °C for 60 s) and a final elongation at 72 °C for 5 min. Duplicate PCR reactions was performed for each sample and the duplicates were pooled after PCR. The forward and reverse tailed primers were designed according to (Illumina, 2015) and contain primers targeting bacteria and archaea 16S gene V3-4 region (Sundberg et al., 2013): 5'-CCTAYGGGRBGCASCAG (341F) and 5'-GGACTACNNGGGTATCTAAT (806R). The primer

241 tails enable attachment of Illumina Nextera adaptors for sequencing in a subsequent PCR. The
242 resulting amplicon libraries were purified using the standard protocol for Agencourt Ampure XP Bead
243 (Beckman Coulter, USA) with a modified bead to sample ratio of 4:5. The DNA was eluted in 33 μL
244 of nuclease free water (Qiagen, Germany). DNA concentration was measured using Qubit™ HS DNA
245 Assay kit (Thermo Fisher Scientific, USA).
246 Sequencing libraries were prepared from the purified amplicon libraries using a second PCR. Each
247 PCR reaction (25 μL) contained 1x PCRBIO HiFi buffer (PCRBiosystems, UK), PCRBIO HiFi
248 Polymerase (1U) (PCRBiosystems, UK), adaptor mix (400 nM of each, forward and reverse) and up
249 to 10 ng of amplicon library template. PCR was run with the following program: initial denaturation
250 at 95 °C for 2 min, 8 cycles of amplification (95 °C for 20 s, 55 °C for 30 s, 72 °C for 60 s) and a
251 final elongation at 72 °C for 5 min. The resulting sequencing libraries were purified using the standard
252 protocol for Agencourt Ampure XP Bead (Beckman Coulter, USA) with a modified bead to sample
253 ratio of 4:5. The DNA was eluted in 33 μL of nuclease free water (Qiagen, Germany). The DNA
254 concentration was measured using Qubit™ HS DNA Assay kit (Thermo Fisher Scientific, USA). Gel
255 electrophoresis using Tapestation 2200 and D1000 screentapes (Agilent, USA) was used to check the
256 product size and purity of a subset of sequencing libraries.
257 The purified sequencing libraries were pooled in equimolar concentrations and diluted to 2 nM. The
258 samples were paired end sequenced (2x301bp) on a MiSeq (Illumina) using a MiSeq Reagent kit v3,
259 600 cycles (Illumina, USA) following the standard guidelines for preparing and loading samples on
260 the MiSeq, as described in Caporaso et al. (2012). 20% Phix control library was spiked in to overcome
261 low complexity issue often observed with amplicon samples.
262 Forward reads were trimmed for quality using Trimmomatic v. 0.32 (Bolger et al., 2014) with the
263 settings SLIDINGWINDOW:5:3 and MINLEN:275. The dereplicated reads cut to 275 bp and
264 clustered using the usearch v. 7.0.1090 -cluster_otus command with default settings. OTU
265 abundances ware estimated using the usearch v. 7.0.1090 -usearch_global command with -id 0.97.
266 Taxonomy was assigned using the RDP classifier (Wang et al., 2007) as implemented in the

parallel_assign_taxonomy_rdp.py script in QIIME (Caporaso et al., 2010), using the MiDAS database v.1.20 (McIlroy et al., 2015). The results were analysed in R (R Core Team, 2015) through the Rstudio IDE using the ampvis package v.1.27.0 (Albertsen et al., 2015).

3.4 Tridimensional successional changes in biofilm

Clean microscopy slides were placed in the central point of channel (corresponding to sampling site C4) with a Polyvinyl chloride (PVC) support and collected overtime (2-7-12 days) to monitor biofilm development, biomass increments in the earlier stages and changes in the tridimensional structure during biofilm maturation. The tridimensional structure, successional changes and microbial colonization were assessed using CARD-FISH technique in combination with Confocal Laser Scanning Microscopy, according to the protocol of Lupini *et al.* 2011. Image elaborations were performed using Imaris 6.2 software (Bitplane AG, Zurich, Switzerland).

3.5 Travertine analysis

Travertine encrustations were collected immediately downstream with respect to each biofilm sampling point at the interface between the channel bottom and water. Travertine samples were analyzed by Scanning Electron Microscopy (SEM, coupled to Energy Dispersive Microanalysis, EDS) and X-ray Powder Diffraction (XRPD). After sampling, the eight collected encrustations (C1 to C8) were manually separated at the binocular microscope according to their color (white, red and green, labelled W, R and G, respectively). When possible, the original texture was preserved. The resulting aliquots were 15 (**Table S1**). In addition, two samples were also collected from the artificial deposits at different times (14 and 21 days) by inserting the slides in the central point of the channel. The aliquots were gently fixed over the stubs for SEM analysis, using a double-sided conductive carbon tape, coated with a graphite layer to ensure their electrical conductivity and analyzed with a SEM ZEISS EVO MA15 (at MEMA – Centro di Servizi di Microscopia Elettronica e Microanalisi, University of Florence), equipped with the Oxford INCA 250 Microanalysis. Backscattered and

293 secondary electron micrographs were registered while the mineral identification was carried out by
294 means of point and raster X-ray EDS microanalysis. Measurements were carried out at an accelerating
295 voltage of 20 KV.
296 The materials considered for the X-ray Powder Diffraction (XRPD) was carried out after gently
297 crushing each sample in an agate mortar and analyzed with a XRD Bruker New D8 Da Vinci powder
298 diffractometer (at CRIST– Centro di Cristallografia Strutturale, University of Florence),employing a
299 Ni-filtered Cu Kα (1.54187 Å) radiation. XRPD patterns were registered at 1,600 W (i.e. 40 kV, 40
300 mA) with a fast multi-channel detector in the 2θ range 10-90°, applying a step size of 0.0205° 2θ.
301 The XRPD data were refined by means of full-profile Rietveld algorithm, using the Fullprof software
302 (Rodriguez-Carvajal J, 1993). The red and green aliquots obtained from C4 (i.e. C4R and C4G,
303 respectively; **Table S1**) were investigated together with a synthetic commercial calcite (Rudi Pont,
304 Turin, Italy). This latter sample was used to calibrate the diffractometer geometry and line shape.
305
306 **3.6 Computational model**
307 Numerical modelling of the geochemical system (surface and bottom fluids) was performed by means
308 of the TOUGHREACT v (Xu and Pruess, 2001; Xu et al., 2006) software, using the default database
309 included in the package (thermoxu.dat; Xu and Pruess, 2001; Xu et al., 2006). The model uses the
310 equation of state EOS2 for water and CO_2 (Pruess et al., 2012). The geochemical model strategy
311 proceeds through a fully kinetic approach. With the kinetic database from Palandri and Kharaka
312 (2004), the mineral specific surface was calibrated against the measured data. The relative
313 permeability and capillary pressure equation was obtained according to Corey (1954), with an
314 irreducible liquid saturation assumed at 0.2. Diffusivity coefficients of CO_2 in water along the vertical
315 section of the channel and from the top of the channel into atmosphere were computed, as a function
316 of temperature, according to Cadogan et al. (2014).
317 The channel was modelled as a material with porosity of 0.9999 and permeability of $1 \cdot 10^{-10}$ m^2, with
318 specific heat and heat conductivity of pure water (1 kJ kg^{-1} K^{-1} and 0.6 W m^{-1} K^{-1}, respectively). A

two-dimensional x-z model, whose dimensions were 110 m long and 10 cm high (plus one more cell for the atmosphere boundary), described the channel. This system was modelled with an x,z grid made of 100 × 21 computational elements. At the end side of the channel (discharge pool), a column of infinite volume cells provided the right boundary condition (i.e. the conditions were constant: T=16.4 °C; P nearly 1 bar accounting for the hydrostatic pressure gradient within the channel). At the left side of the model (inlet pool), a column (20 cells) injects a constant flow rate of 0.035 kg s^{-1} of H_2O at $2.7867 \cdot 10^5$ J kg^{-1} enthalpy, and $1.52 \cdot 10^{-5}$ kg s^{-1} CO_2 at $1.528 \cdot 10^6$ J kg^{-1} enthalpy, corresponding to the flow rate measured at *PC* at 52.7 °C. The chemical composition of the injected water corresponds to that analyzed in C1 (see previous paragraph) and was used to model the chemical evolution of the channel. The atmospheric boundary was set as infinite volume elements at 1.103×10^5 Pa pressure, 16.4 °C temperature and 40 Pa CO_2 partial pressure (corresponding to 400 ppm of CO_2). The measured temperature and CO_2 profiles along the channel were used to validate the model. The only calibrated variable was the reactive surface of the main mineral phase of the system, i.e. calcite.

4. Results

4.1 Physical-chemical characteristics of waters and dissolved gases

A strong decrease in water temperature was observed along the *PC* channel, passing from 52.4 (C1) to 16.4 (C8) °C. Differently, an increase in DO values was observed along the channel, with values from 1.84 to 9.08 mg/L (**Table 1**). Similarly, pH increased from C1 to C4 (from 7.25 to 8.40) and then ranged between 8.63 in C5 and 8.61 in C8 (**Table 1**).

The sampled waters were characterized by a Ca-SO_4(HCO_3) composition, with TDS (Total Dissolved Solids) values progressively decreasing along the channel, i.e. from 3.2 to 2.8 g/L, mainly due to a decrease in Ca^{2+} and HCO_3^- (**Table 1**). Similarly, an overall decreasing trend was also observed in the concentrations of trace species, such as Fe, Mn and Ba, from C1 (40, 35 and 46 µg/L, respectively) to C7 (6.9, 20 and 25 µg/L, respectively), whereas they slightly increased in C8 (**Table 1**). Similarly,

NH_4 concentration also progressively decreased along the channel, whereas NO_2 showed a regular, though increasing trend, such as that of TOC (**Table 1**).

Among dissolved gases, a sharp decrease along the channel was recorded for dissolved CO_2, i.e. from 9.86 to 4.46 mmol/L, as well as CH_4, from 0.089 to 0.048 mmol/L (**Table 1**). Differently, O_2 concentrations increased of one order of magnitude along the channel, i.e. from 0.005 to 0.068 mmol/L (**Table 1**).

The carbon isotopic composition of TDIC and dissolved CO_2 increased along the channel, ranging from +1.88 and -3.86 ‰ vs. V-PDB in C1, respectively, to +4.90 and -0.69 ‰ vs. V-PDB in C3, respectively, and then they were clustering around +5.26 and -0.05 ‰ vs. V-PDB from C4 to C8, respectively (**Table 1**).

Sample		C1	C2	C3	C4	C5	C6	C7	C8
Distance	**m**	0	14	28	42	56	70	84	100
T	**°C**	52.4	42.6	39.1	30.8	25.7	23.5	20	16.4
DO	**mg/L**	1.84	5.84	6.39	8.02	8.22	8.42	8.41	9.08
pH		7.25	7.76	8.16	8.4	8.63	8.62	8.69	8.61
TDS	**g/L**	3.20	3.24	2.96	2.92	3.01	2.96	2.85	2.79
HCO_3	**mg/L**	1180	1243	987	965	1007	982	885	854
F	**mg/L**	2.60	2.40	2.02	2.73	1.96	1.98	1.73	1.88
Cl	**mg/L**	17.7	21.6	21.5	23.3	21.7	21.7	22.9	22.2
Br	**mg/L**	0.023	0.082	0.033	0.03	0.066	na	na	0.104
NO_3	**mg/L**	0.065	0.102	na	na	0.074	0.057	0.490	0.340
NO_2	**mg/L**	0.010	0.007	0.020	0.030	0.003	0.026	0.026	bdl
NH_4	**mg/L**	1.417	1.159	0.863	0.708	0.799	0.631	0.657	0.631
SO_4	**mg/L**	1153	1175	1182	1180	1196	1187	1199	1186
Li	**mg/L**	0.025	0.021	0.021	0.015	0.022	0.015	0.020	0.018
Na	**mg/L**	38.8	35.9	37.6	37.5	38.9	40.1	37.5	35.1
K	**mg/L**	41.5	38.9	39.5	39.9	41.0	38.5	41.1	36.2
Mg	**mg/L**	136	131	133	130	135	135	132	128
Ca	**mg/L**	627	593	561	541	569	551	533	525
Mn	**µg/L**	35	33	27	23	23	28	20	22
Fe	**µg/L**	40	21	19	7.1	6.8	11	6.9	33
Co	**µg/L**	0.3	bdl	0.2	0.2	bdl	bdl	bdl	bdl
Ni	**µg/L**	3.4	3.1	3.2	2.8	2.7	3.4	1.7	2.6
Cu	**µg/L**	5.4	5.4	4.9	5.0	5.0	6.6	5.1	5.1
Zn	**µg/L**	6.1	6.2	3.3	4.7	5.4	14	3.1	5.7
Ba	**µg/L**	46	44	35	26	28	26	25	44
Sb	**µg/L**	7.5	6.4	6.7	2.8	2.7	3.4	bdl	5.7
As	**µg/L**	176	215	209	219	202	193	162	187
TOC	**mg/L**	0.23	0.34	0.35	0.70	0.44	0.22	0.47	0.53
δ^{13}C-TDIC	**‰ vs. V-PDB**	1.88	3.76	4.90	5.07	5.00	5.56	5.46	5.22
CO_2	**mmol/L**	9.86	9.47	9.16	8.06	6.58	5.47	5.45	4.46
N_2	**mmol/L**	0.51	0.56	0.55	0.52	0.51	0.55	0.58	0.61
CH_4	**mmol/L**	0.089	0.079	0.081	0.075	0.069	0.056	0.051	0.048
Ar	**mmol/L**	0.015	0.018	0.020	0.013	0.013	0.014	0.014	0.015
O_2	**mmol/L**	0.005	0.005	0.009	0.009	0.011	0.031	0.051	0.068
He	**mmol/L**	0.000028	0.000025	0.000022	0.000021	0.000025	0.000018	0.000016	0.000016
δ^{13}C-CO_2	**‰ vs. V-PDB**	-3.86	-2.80	-0.69	-0.03	na	-0.23	0.23	-0.15

Table 1 Physical-chemical and isotopic (δ^{13}C-TDIC and δ^{13}C-CO_2) features of the water and dissolved gas samples collected along the PC channel; na: not analyzed.

354

355 **4.2 The *PC* channel: physical chemistry and mineral precipitation modeling**

356 A numerical model was defined by assuming a purely abiotic evolution of the water parameters
357 provided by the spring supply. The validation of the thermal and flow rate model was carried out by
358 comparing the theoretically predicted temperature and the dissolved CO_2 parameters with those

effectively measured in the field. The data reported in **Fig. 2a** evidence a very good agreement between experimental and computed temperatures at increasing distances from the spring. Since flow rate affects the thermal exchange with atmosphere, thus governing the cooling of the channel, the calculated thermal profile allowed the correct prediction of the temperature, evaluated at 1 cm from the bottom of the channel.

The dissolved CO_2 amount was regulated by both exsolution towards the atmosphere boundary and vertical diffusion of CO_2 in water. Similarly to the measured and computed temperatures, the model accurately reproduced all experimental evidences (**Fig. 2b**).

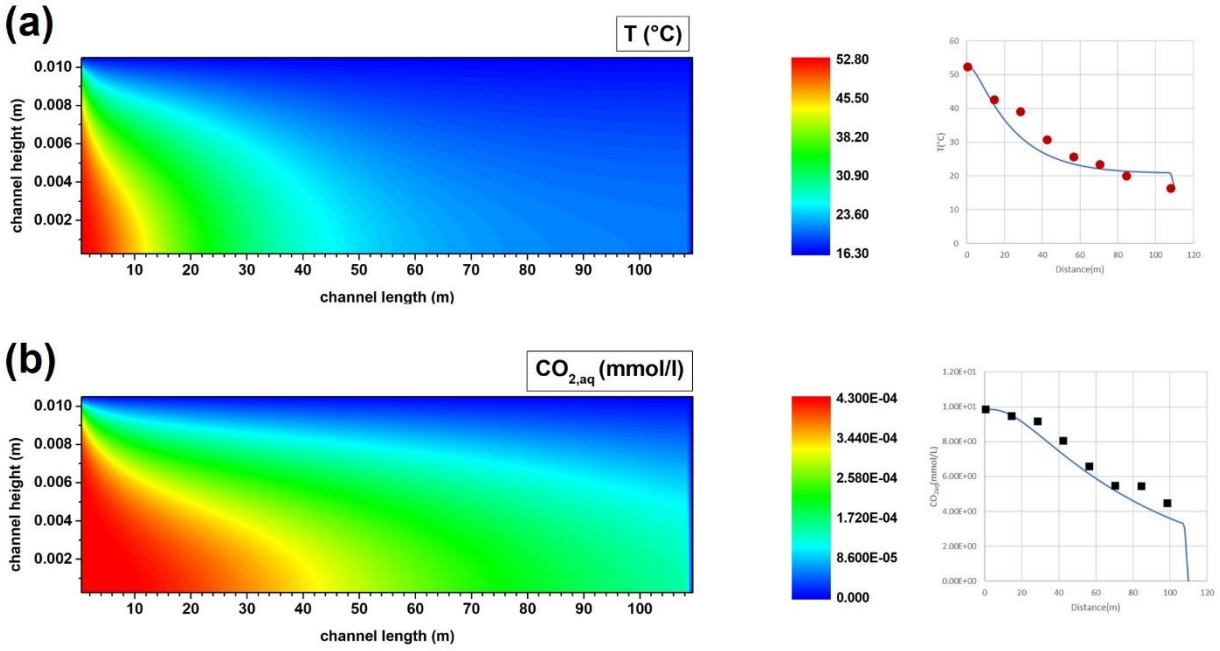

Figure 2 Results of the numerical model of the channel: (a) temperature and (b) dissolved CO_2. In the inset, the comparison of the considered parameter, evaluated at 1 cm from the bottom of the channel (blue line), with the corresponding experimental measurement (points), listed in Table 1.

Once validated, the model can predict theoretical diffusion and transport properties of chemical species involved in both solution equilibria and precipitation of solid phases. The behavior of HCO_3^- and Ca^{2+} can be modelled by a kinetically controlled calcite precipitation (**Fig. 3a-c**). The kinetics of this process was accounted through a reaction surface of 1.105×10^6 m^2/m^3, that corresponded to a grain size of ~30 µm. This size represented a maximum value, and it could be reduced to some microns taking into account additional factors such as packing, biofilm occlusion, active sites on the

surface (e.g. Murphy et al., 1989; Steefel and Maher, 2009). The computed calcite grain size was then compared with that measured by SEM. Calcite in each travertine sample was found in different aggregates. However, individual grains were rarely exceeding 20 µm. In contrast, high surface grain aggregates of definitely lower dimensions were almost frequent (see §4.6). Accordingly, a good match between the grain size evaluated by the numerical model and that observed in the collected samples can be assessed.

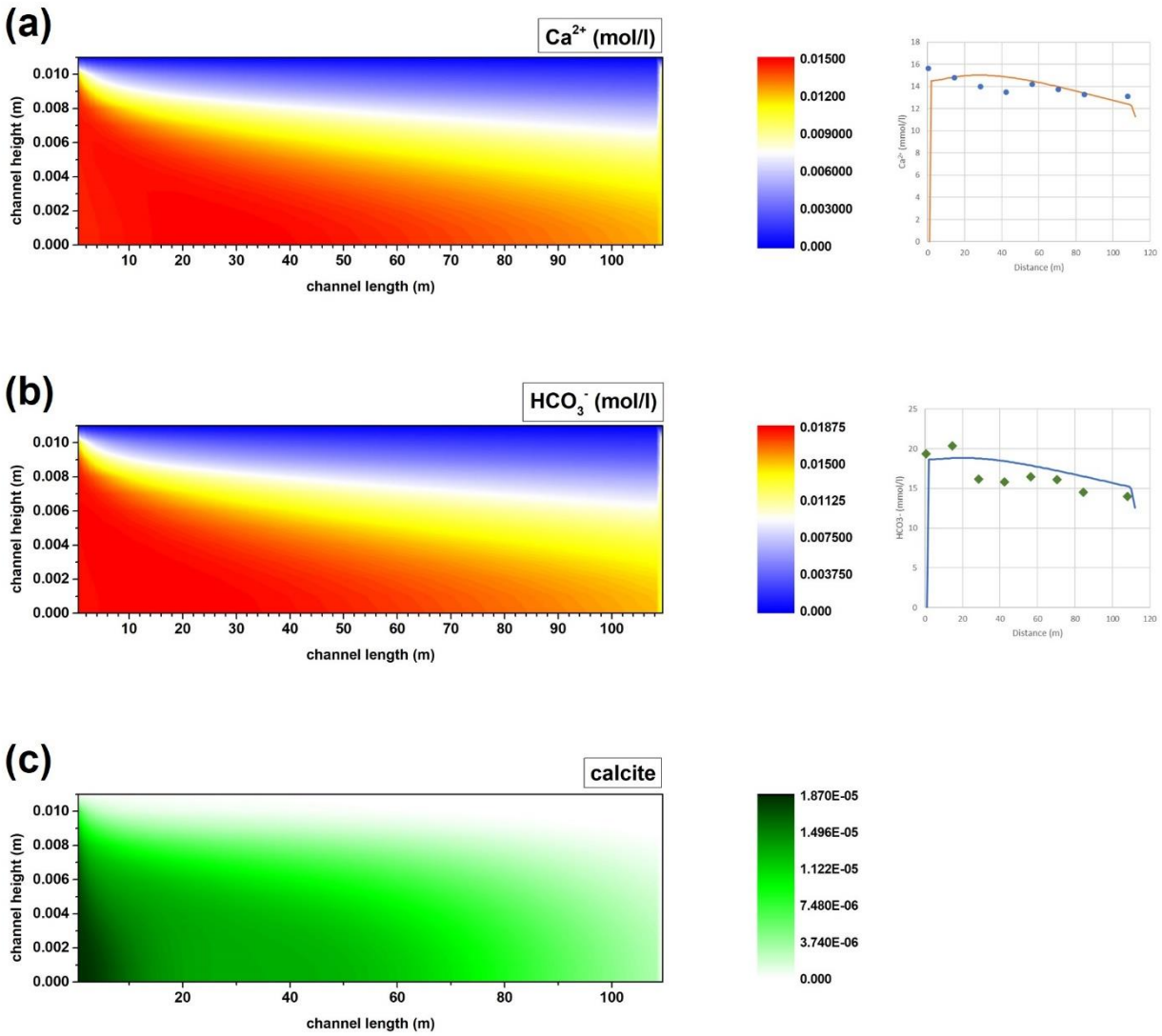

Figure 3 Results of the numerical model of the channel: (a) Ca^{2+} and (b) HCO_3^-. In the inset, the comparison of the considered parameter, evaluated at 1 cm from the bottom of the channel (blue line), with the corresponding experimental measurement (points), listed in Table 1. (c) Volume fraction of precipitated calcite.

Concerning other ions, i.e. F^- and Cl^- and cations, such as Li^+, Mg^{2+}, K^+, and Na^+, the experimental results and those provided by the model point to a nearly constant behavior. This can be explained with the fact that (i) their salts are highly soluble and (ii) no reactions affect these ions.

An exception to this general trend is provided by SO_4^{2-}, being possibly involved in gypsum precipitation reaction. The model predicted that sulfate concentration evolved towards a layered pattern (**Fig. S1a**). However, the total amount of dissolved sulfate was not generally changing. This finding is in line with the saturation index values that were calculated along the whole channel (**Fig. S1b**). According to our model, gypsum precipitation did not occur due to the low saturation index (**Fig. S1b**). Similar considerations can be done for amorphous SiO_2 and CaF_2, which are frequently precipitating from the Central Italy thermal springs (Allen et al., 2000).

4.3 Prokaryotic abundance and community structure in water

Total prokaryotic abundance in water samples increased from 6.8×10^5 cells/mL to 8.2×10^5 cells/mL along the channel (**Table S2**). A slight decrease of cells with High Nucleic Acid content (HNA) was observed from the origin to the end of the channel. Notably, HNA cells represented 87.8% of total cells in C1 and 71.9% in C8. Cytograms showed high cytometric similarity between water samples highlighting a highly similar microbial community along the channel. Accordingly, CARD-FISH analysis revealed a similar microbial community composition in water column along the channel (**Fig. 4a**). The main microbial component in water samples belonged to bacteria domain (on average 79.3 % of total DAPI-stained cells) mainly affiliated with *Proteobacteria* (**Fig. 4a**). *Gammaproteobacteria* was the predominant group along the whole channel showing abundances between $1.2 \times 10^5 \pm 5.1 \times 10^3$ and $5.3 \times 10^5 \pm 2.0 \times 10^4$ cells/mL (range: 16.7 - 77.1 % of DAPI-stained cells). On average, *Alpha-*, *Beta-* and *Deltaproteobacteria* represented 7 % of total prokaryotic abundance. The other bacterial groups represented less than 2.2 % of total cells. Meanwhile, 15.4 % of total prokaryotic

cells (on average) belonged to *Archaea*, with a cell abundance ranging between $4.1 \times 10^4 \pm 1.2 \times 10^3$ cells/mL and $1.9 \times 10^5 \pm 6.4 \times 10^3$ cells/mL.

The outputs from high-throughput sequencing were in line with the results generated by CARD-FISH analysis. In particular, a total of 57,943 reads were generated by C1, C4, and C7 water samples. These reads resolved into 239 OTUs. Overall, *Proteobacteria* was the most abundant phylum, mainly represented by *Gammaproteobacteria* affiliated with genus *Thiofaba* (~85% of total OTUs) (**Fig. 4b**). *Epsilonproteobacteria* represented around 9.2% of total reads. *Archaea* represented on average less than 1% of total reads. A low level of biodiversity was found in water samples with Shannon index values ranging between 0.6 and 0.8 and very similar Simpson index values (range: 0.26 - 0.30).

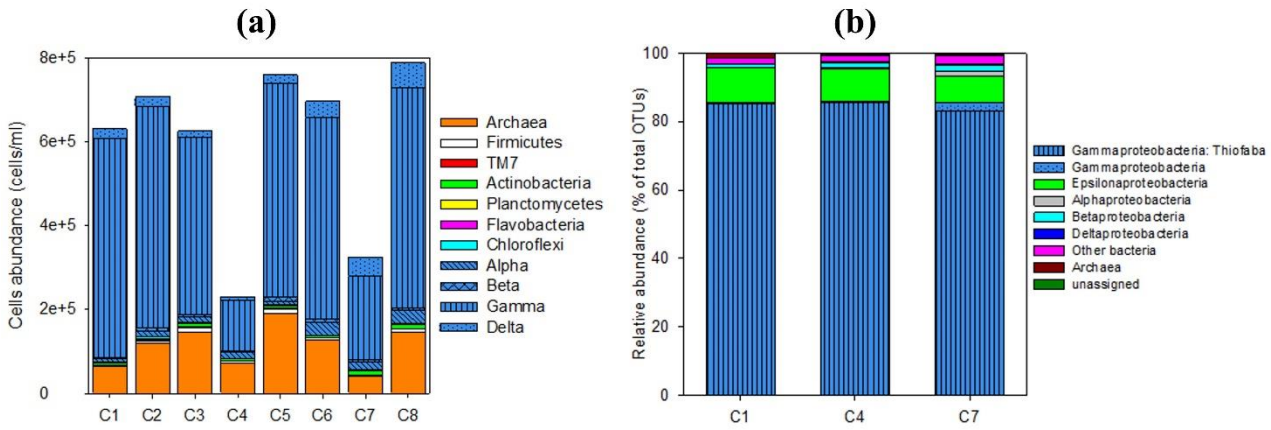

Figure 4 Water: (a) Abundance of phylogenetic taxa (Archaea and main phyla within Bacteria) and single classes within Proteobacteria (in blue) in the different water sampling points. (b) OTUs relative abundance in water samples estimated by NGS. Bacterial taxa accounting for less than 1% of total composition were classified as 'Other bacteria'.

4.4 Prokaryotic abundance and community structure in biofilm

Along the channel, total prokaryotic abundance tended to decrease in superficial biofilm layers whereas it increased in those sub-superficial (**Fig. 5a**). In particular, values decreasing from 3.8×10^9 cells/g to 4.0×10^7 cells/g were observed in superficial layers from C2 to C8 samples. In contrast, increasing values from 5.2×10^7 cells/g to $8.8. \times 10^7$ cells/g were observed in sub-superficial layers. The microbial communities were dominated by *Bacteria* in both the superficial and sub-superficial layers representing on average the 90 % of total prokaryotes estimated by CARD-FISH. Among

bacterial cells, *Cyanobacteria* were highly abundant in the superficial layers showing values from 2.7 × 10^9 ± 3.0 × 10^7 cells/g in C2 to 1.9 × 10^7 ± 3.5 × 10^6 cells/g in C8 (**Fig. 5b**). Lower cyanobacterial abundances were observed in the sub-superficial layers with an average value of 1.2 × 10^7 ± 7.1 × 10^6 cells/g. The various classes within *Proteobacteria* counted together on average 1.3 × 10^8 ± 1.4 × 10^8 cells/g and 3.1 × 10^7 ± 2.1 × 10^7 cells/g in the superficial and sub-superficial layers, respectively. High-throughput sequencing generated a total of 142,563 reads in the C1, C4, C7 and C8 superficial and sub-superficial biofilm layers that resolved into 949 OTUs. The results showed a high microbial diversity among biofilm samples. The Shannon and Simpson indexes ranged between 2.4 and 2.7 and 0.8 and 0.9 respectively.

OTUs affiliated with *Cyanobacteria* were more abundant in superficial layers (on average 37.3 %) than in sub-superficial ones (on average 13.0 %) (**Fig. 5c**). In particular, these OTUs mainly belonged to genera *Spirulina* (around 35% in C4 and C7 superficial biofilm), *Leptolyngbya* (on average 8.4 % in superficial layer and 1.8 % in sub-superficial one), and *Fischerella* (up to 7.7 % in C4 sub-superficial biofilm). Overall, members of *Proteobacteria* represented on average around 20 % of total reads in biofilm samples. In particular, OTUs affiliated with *Alphaproteobacteria* were the most abundant in both superficial and sub-superficial biofilms. Specifically, they mainly belonged to orders *Rhodobacterales*, *Rhodospirillales*, and *Sphingomonadales*. Furthermore, a high abundance of OTUs affiliated with *Rhodomicrobium*, a genus belonging to order *Rhizobiales* within *Alphaproteobacteria*, was mainly observed in C1 site (14.8 %). OTUs affiliated with *Gammaproteobacteria* represented on average 3.4 % and 1.7 % of total OTUs in superficial and sub-superficial layers, respectively.

The phylum *Chloroflexi* represented on average 8.8 % of total OTUs in superficial biofilms and up to 43.7 % in sub-superficial layers. These OTUs were mainly affiliated with family *Anaerolineaceae* in superficial layer and with genus *Roseiflexus* in sub-superficial one. Members of this phylum were highly abundant mainly in sub-superficial biofilm in C7 site. OTUs affiliated with phylum *Bacteroidetes*, mostly belonging to family *Saprospiraceae*, increased along the channel up to 21.6 % of total OTUs in site C8. The retrieved OTUs affiliated with phylum *Chlorobi* represented on average

2.6 % of total OTUs in both the superficial and sub-superficial layers, with the sole exception of the C2 superficial layer in which members of *Chlorobiaceae* represented up to 12.1 % of total OTUs. Concerning the *Archaea*, *Thaumarchaeota* represented between 14.9 % and 41.0 % of total reads in C1 and C4 sub-superficial layer, respectively. In the other biofilm samples, the OTUs belonging to archaea domain represented less than 0.5 % of total reads.

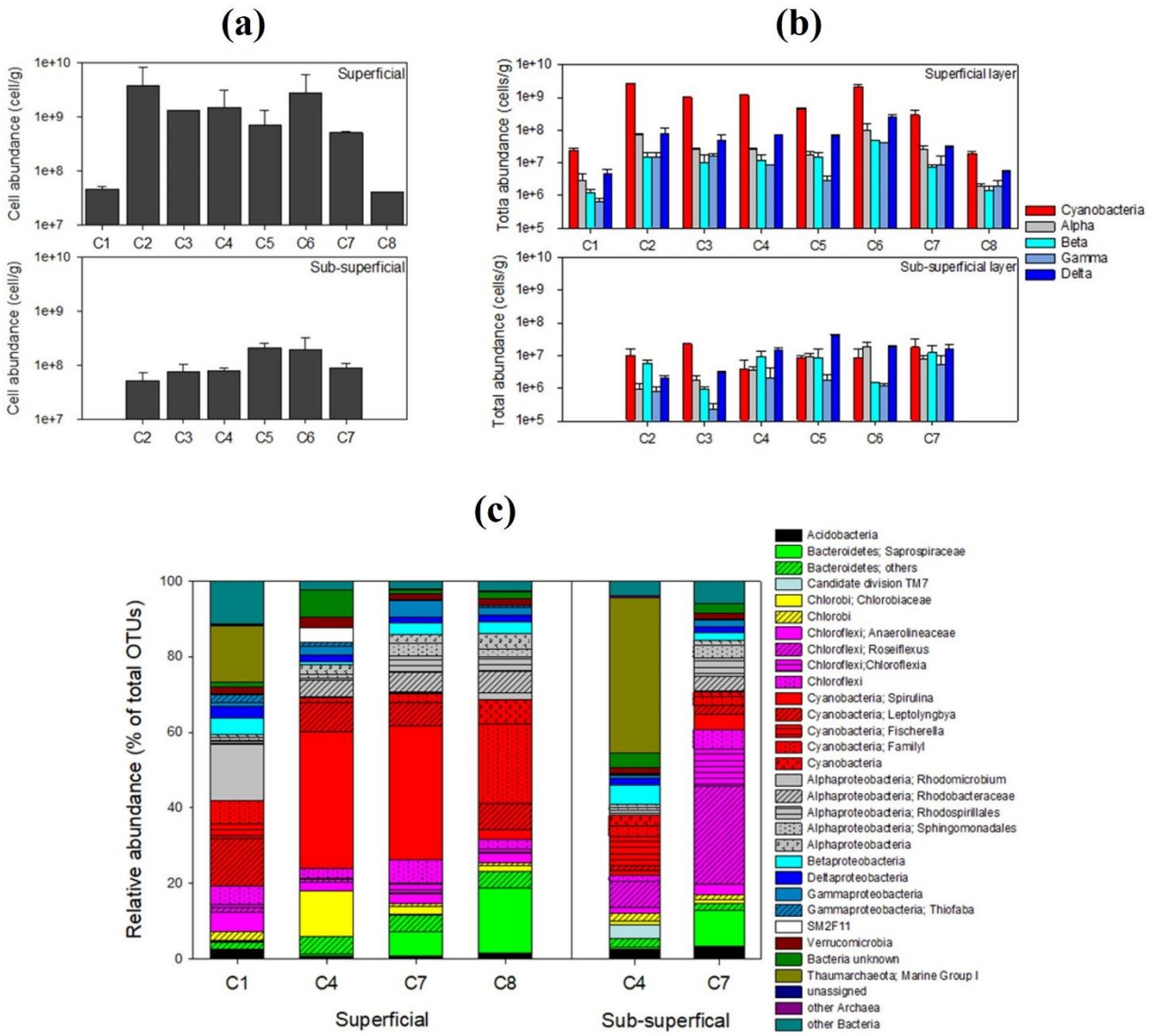

Figure 5 Biofilm: (a) Total prokaryotic abundance in superficial and sub-superficial biofilm samples. (b) Total abundance of Cyanobacteria and single classes within Proteobacteria in superficial and sub-superficial biofilm samples. (c) OTUs relative abundance in biofilm samples estimated by NGS. Clusters making up less than 1 % of total composition were classified as 'other Bacteria' or 'other Archaea'.

4.5 Tridimensional structure and successional changes of biofilm

Development, biomass increments and three-dimensional structure of biofilm growing on microscopy slides placed on the central point of the channel (corresponding to sampling point C4) were observed by combining CARD-FISH and CLSM. After 2 and 7 days, CLSM examination revealed biofilm assemblages with similar microbial community equally represented by filamentous *Cyanobacteria*, and other prokaryotes (**Fig. 6**). After 12 days, a highly complex and multi-stratified biofilm was observed, with a high amount of filamentous spirulina-like *Cyanobacteria*, dominating the microbial community. Within the dense network of filamentous autotrophs, non-pigmented prokaryotic cells were also visible.

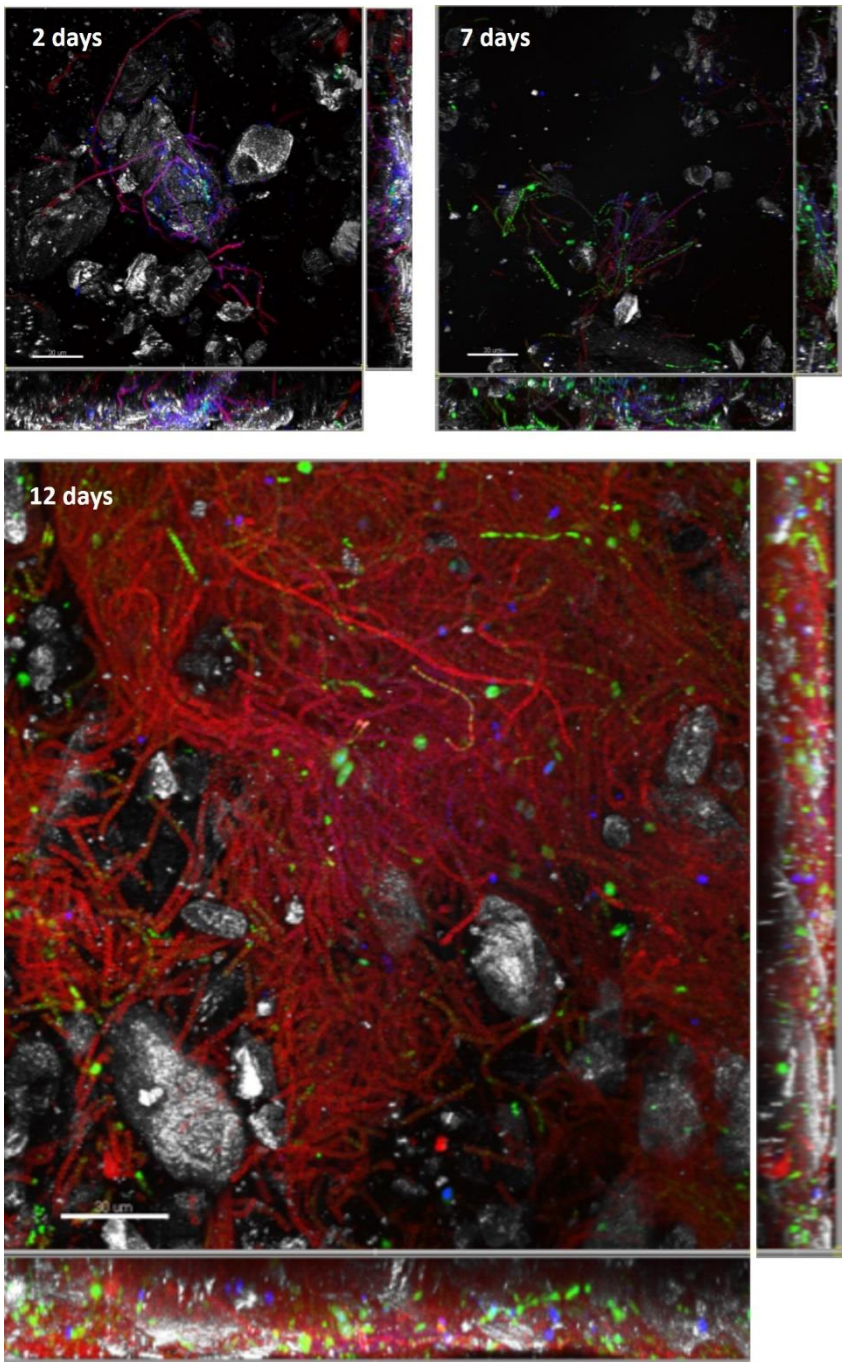

Figure 6 CLSM combined images showing the spatial distribution (X−Y, X−Z, and Y−Z planes) of Bacteria (green), Cyanobacteria (red) and other prokaryotes (blue) identified by CARD-FISH in biofilms. The hybridized bacterial cells were excited with the 488 nm line of an Ar laser (excitation) and observed in the green channel from 500 to 530 nm (emission). Calcite crystals were visualized by their reflection signal (405 nm line of a diodo laser) and appear of gray color.

467

468 **4.6 Mineralogical features**

469 Three mineralogical phases were recognized throughout the channel. Calcite was found in two

470 apparently different and coexisting morphologies. The first one exhibited a rhombohedral or, more

rarely, scalenohedral habitus (**Fig. 7a**). The crystals were almost homogeneous with an average size of about 5 μm and displayed an euhedral aspect. Such calcite was significantly abundant in the C1 precipitate although it was recorded throughout the whole channel. The second, and largely more frequent, calcite facies was a shrub precipitate in which the evolution of the crystal(s) occurred through the surface uptake by rhombohedral lamellae (**Fig. 7b**). In many cases, calcite individual grains were no single crystals, but aggregates of many individuals. Moreover, the overall surface of the grains appeared highly structured and rough (**Fig. 7c and d**). The individual grains were significantly bigger than those of euhedral calcite. All samples but C1 exhibited this kind of mineralization, irrespectively to the type of sample (green, red, or white).

Both calcite precipitates exhibited consumption from either the crystal edges or circular pits on the crystal surfaces. These evidences were recorded in all the samples, although their presence was reduced at >40 °C (C1 and C2).

Occasional, though not infrequent, findings of gypsum precipitates were also observed. All precipitates showed a unique common morphology, i.e. aggregates of relatively small crystals, with apparent traces of the {010} cleavage, assembled through multiple branching scheme, typical of fractal crystallization (Van Driessche et al., 2019; **Fig. 7e**). Moreover, these aggregates grew up to relevant dimensions (up to 50 μm in linear dimension) and appeared randomly but unevenly distributed in the precipitate (**Fig. 7f**). In particular, gypsum precipitates were found always associated to abundant biofilm occurrences. Crystal surfaces were well formed, displaying neither consumption nor pitting evidences.

Finally, the third identified mineral phase was fluorite, with the typical cubic habitus of 5-10 μm in size (**Fig. 7d**). Although its seldom presence in the samples, all observed crystals seemed well formed, apparently unrelated to the mineralogical context where they were recognized, and sometimes clustered in small regions of the samples. The fluorite crystals were perfectly euhedral, without evidence of active re-dissolution processes.

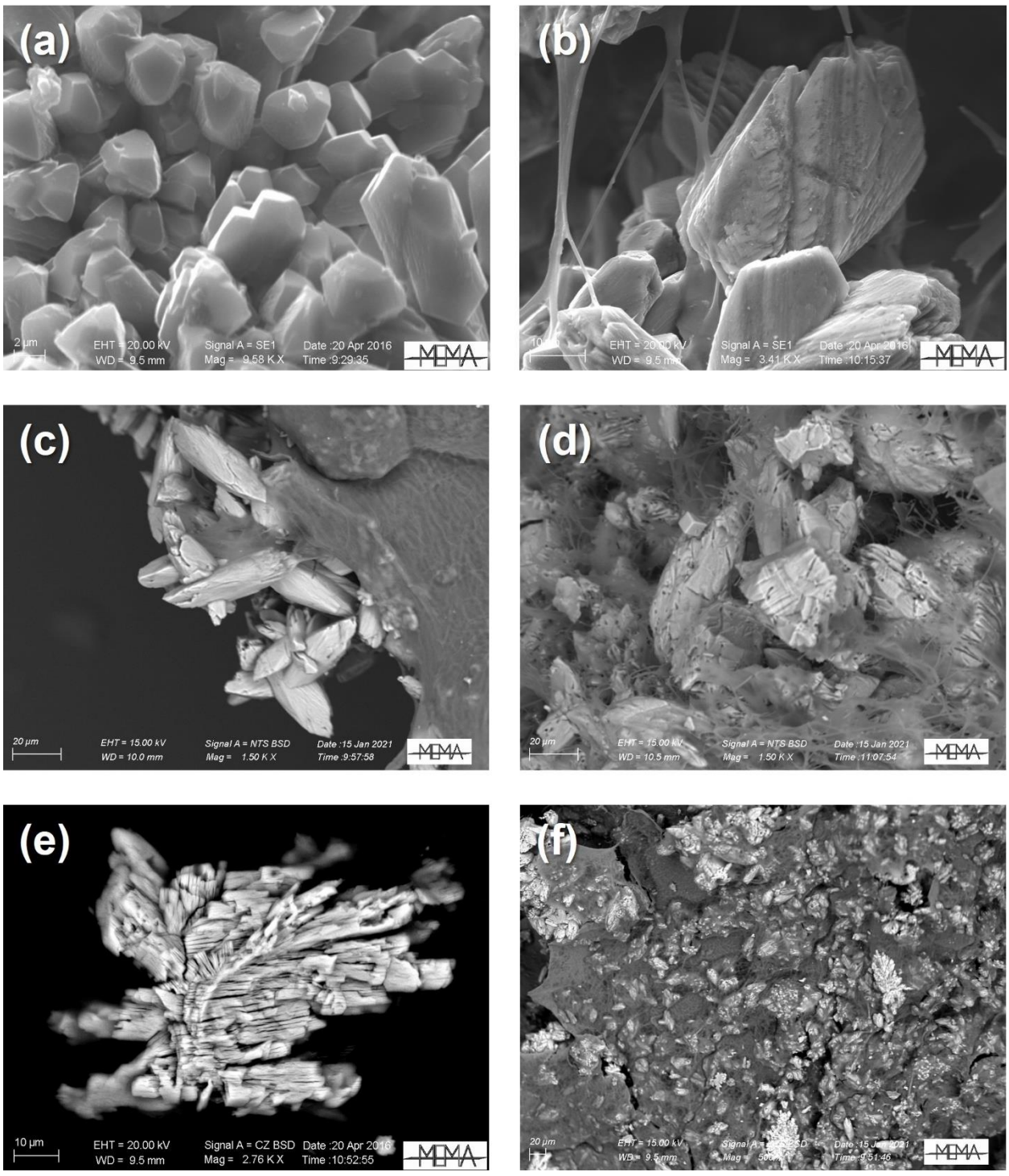

Figure 7 Secondary (a,b) and Backscattered (c-f) electron micrographs of representative regions of the investigated samples: (a) C1W (Magnification: 9580X); (b) C3G (3410X); (c) C2R (1500X); (d) C5G (1500X); (e) C3R (2760X); (f) C2R (500X).

All samples but C1 displayed extensive evidence of biofilm. This provided a relevant network among all types of precipitated minerals, as it can be devised by comparing secondary and backscattered electron micrographs (**Fig. 8a-c**). In the white-colored encrustations (i.e. in C7W and C8W), biofilms were less extended, but still present (**Fig. 8d**). Regarding the relationships with the four types of

501 described minerals (euhedral and shrub calcite, gypsum, fluorite), no specific relationship occurred
502 between biofilm and euhedral calcite, gypsum, fluorite. Their spatial co-localization resulted just from
503 a juxtaposition of spatially confined events. Conversely, the mutual relationships between biofilm
504 and shrub calcite were completely different and more complex (**Fig. 7b and 8e**): in certain cases, the
505 grains were completely enveloped by biofilm whereas, more frequently, they were interconnected by
506 bridges of organic matter. Overall, the mutual relationships between biofilm and shrub calcite
507 appeared to be not occasional.

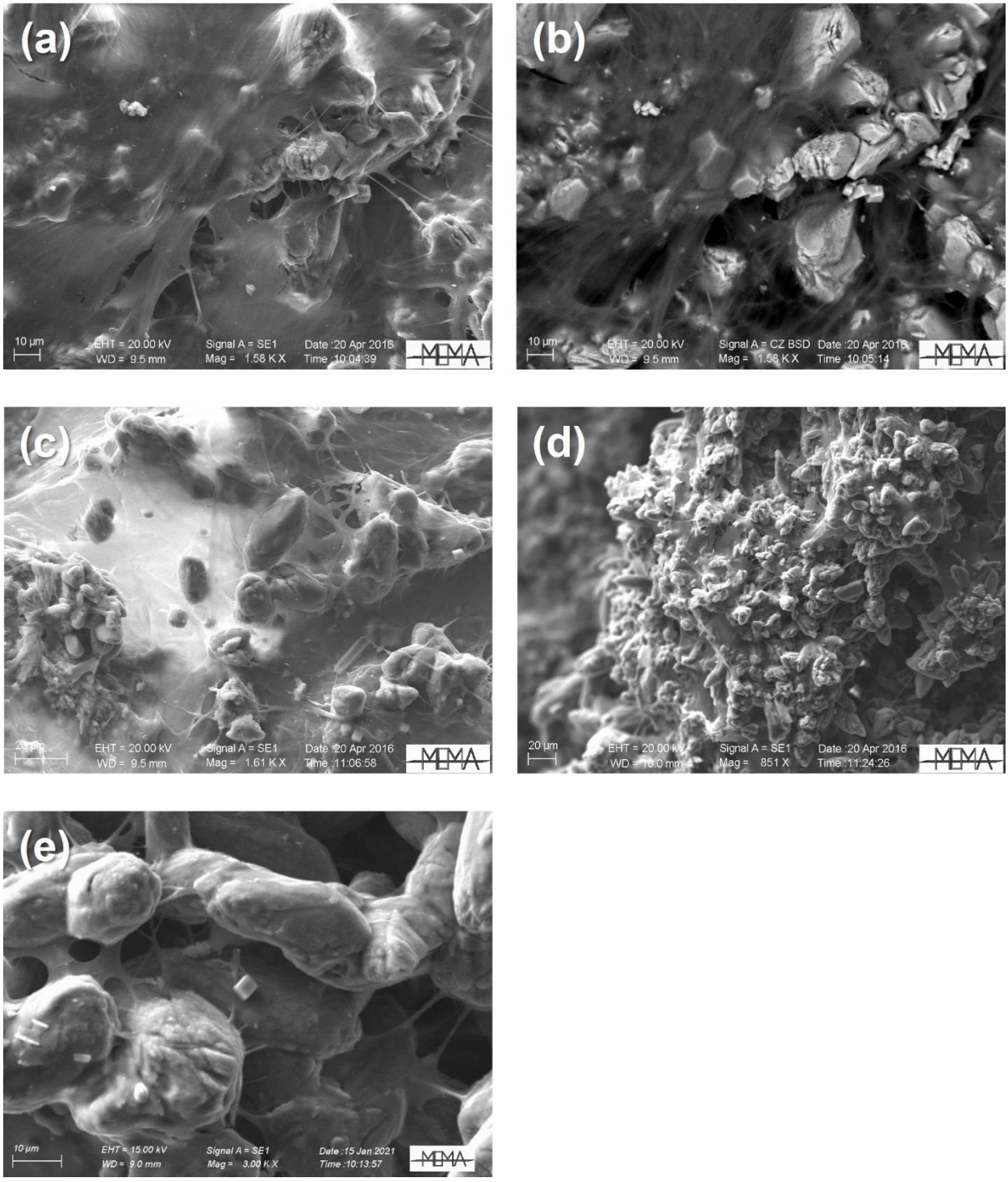

Figure 8 Secondary (a,b-e) and Backscattered (b) electron micrographs of representative regions of the investigated samples: (a) C3G (Magnification: 1580X); (b) C3G (1580X); (c) C8G (1610X); (d) C8W (851X); (e) C7G (3000X).

508

509 The two additional samples obtained by exposing at the water flux two glass slides near the C4
510 sampling point revealed interesting features about the processes under which the travertine
511 encrustation form. The two samples were exposed at different times, and the difference in their micro-
512 morphological details could be ascribed to the temporal evolution of the encrustation over the slide.

513 The main difference (**Fig. 9a-b**) is the net increase of biofilm occurrence in the sample. In the 14-day
514 slide biofilm is scarce whereas in the 21-day slide it appeared abundant. Concerning calcite precipitate
515 morphology, at intermediate time both the rhombohedral and the shrub facies are concurring, with
516 poor evidence of crystal weathering (**Fig. 9a**). Weathering, as well as the occurrence of topological
517 relationships between calcite crystals and biofilm (already observed by confocal microscopy) are the
518 main features of the calcite precipitates (almost exclusively shrub) in the 21-day slide (**Fig. 9b**).
519 Interestingly, in the 14-day slide also spherules of aragonite needles, already described by Allan et
520 al. (2000) for the nearby Zitelle spring system, were identified (**Fig. 9a**).

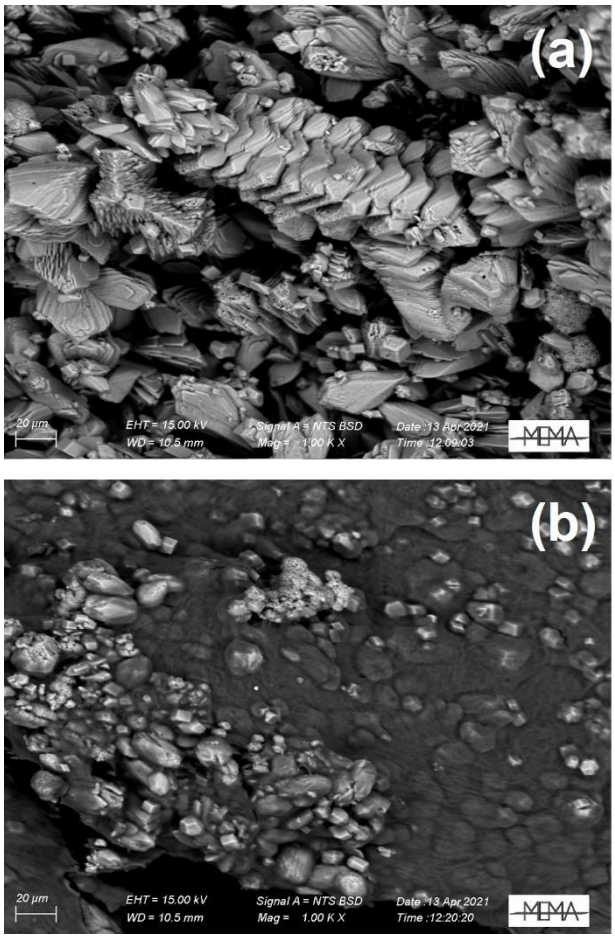

Figure 9 Backscattered electron micrographs of two representative regions of travertine precipitated after (a) 14 days and (b) 21 days over the glass slide. Magnification: 1000X.

521

522 XRPD analysis on differently colored aliquots (C4R and C4G) showed a simple mineralogy, being
523 largely dominated by calcite (**Fig. S2**). Weak additional reflections in the 25-35 2θ range can be
524 attributed to quartz and another carbonate, e.g. dolomite. These results agree with the findings by Di

525 Benedetto et al. (2011), where travertine encrustations were investigated without dividing them into
526 colored aliquots. A refinement of the lattice constants, operated by means of the Rietveld method,
527 provided the results shown in the **Table S3**. The calcite lattice parameters, the relative c/a ratio and
528 the cell volume appear rather similar in the two aliquots. Conversely, when compared with analogous
529 parameters described for a pure inorganic calcite (Graf, 1961), a net lattice strain coupled to a slight
530 increase of the cell volume can be noticed. This strain was attributed to biomediated precipitation
531 processes (Di Benedetto et al., 2011). Accordingly, the red and green travertine encrustations
532 appeared very similar in terms of mineralogical composition and structural features.

533

534 **5. Discussion**

535 **5.1 The geochemical system of the *PC* channel**

536 Water and dissolved gas chemistry from the *PC* channel was consistent with those reported by
537 previous studies (Di Benedetto et al., 2011). The Ca-SO_4(HCO_3) facies is typical of thermal waters
538 circulating in the Vicano-Cimino Volcanic District, affected by water-rock interactions with the
539 Mesozoic carbonate sequence and Triassic anhydrites (e.g. Minissale, 2004; Cinti et al., 2014).
540 Despite the limited spatial scale, the geochemical features evolved along the PC channel with a sharp
541 temperature gradient associated to chemical changes. The water-atmosphere exchange led to a
542 progressive increase in dissolved O_2 concentrations as the distance from the water spring increased,
543 favoring the oxidation of reduced species as indicated by the decrease in NH_4^+ concentrations coupled
544 with an overall increase in NO_3^- contents. On the other hand, the rapid exsolution of CO_2 towards the
545 atmosphere drove calcite precipitation along the *PC* channel, resulting in a progressive decrease in
546 Ca^{2+} and HCO_3^- ions, as also supported by the numerical model. Accordingly, CO_2 degassing was
547 expected to be the main driving factor of travertine precipitation, as observed in similar systems (e.g.
548 Dupraz et al., 2009). Coherently, the carbon isotopic composition of both dissolved CO_2 and TDIC
549 showed a progressive increase along the *PC* channel, being largely controlled by the fast CO_2

exchange with the atmosphere, as reported by Di Benedetto et al. (2011). The latter authors also evidenced the occurrence of an out-of-equilibrium isotopic fractionation process between travertine and dissolved carbon species, attributed to either kinetically controlled inorganic calcite precipitation or biomineralization processes. On the other hand, the SO_4^{2-} concentrations showed no significant variations along the channel, in agreement with the thermodynamic model, which predicted that gypsum precipitation did not occur along the channel.

5.2 Microbial assemblages in waters and biofilms

Microbiological characteristics in water samples were shaped by the physicochemical features of the *PC* channel. HNA cells, which are often considered as the most active fraction (Lebaron et al., 2001), showed a relatively high abundance in the initial section of the *PC* channel, suggesting a higher microbial activity with respect to the final section. The decrease of HNA cells along the channel was likely related to the transition from an anaerobic/anoxic high temperature aquatic environment to aerobic and low temperature conditions. Overall, hot springs are characterized by a low biodiversity due to their extreme conditions in terms of temperature and chemical characteristics (Kemp and Aller, 2004; Chiriac et al., 2017). In this study, low levels of biodiversity were observed in the water columns probably due to the harsh environmental conditions more suited to pioneer/resistant species (Piscopo et al., 2006; Giampaoli et al., 2013; Valeriani et al., 2018). Accordingly, the microbial community in the water column analyzed in this study was dominated by *Thiofaba* genus (*Gammaproteobacteria* class), able to grow under strict aerobic conditions with a chemolithoautotrophic metabolism. Members of this genus are known to oxidize sulfur compounds by utilizing H_2S as electron donor for CO_2 reduction (van Gemerden, 1993) and are widely reported in hot springs worldwide (e.g. Gulecal-Pektas and Temel, 2017; Gumerov et al., 2011; Huang et al., 2011; Mori and Suzuki, 2008; Valeriani et al., 2018). Furthermore, the occurrence of *Epsilonproteobacteria* in the water column confirmed the involvement of microbial community in the sulfur cycle along the channel. Members of this class have indeed been proposed to being actively

involved in sulfur cycling, constituting one of the major sulfur-oxidizers microbial group in high temperature thermal springs (Campbell et al., 2006).

Although *Thiofaba* genus and *Epsilonproteoboacteria* were highly abundant in water, their occurrence in the biofilm samples was very low. Remarkably, the complex microbial community inhabiting the biofilm along the channel was mainly composed by phototrophic microorganisms, in line with those previously observed in other hot springs (Bilyj et al., 2014; Coman et al., 2013; Portillo et al., 2009; Stal et al., 2017; Wang et al., 2013). In particular, the predominant metabolic pathway was the oxygenic and anoxygenic phototrophy driven by members of *Cyanobacteria*, *Chloroflexi*, *Chlorobi* and *Alphaproteobacteria* (Coman et al., 2013). A stratified microbial community was retrieved in biofilm along the channel, as previously observed in hot spring-bearing microbial mats; in particular, the aerobic photoautotrophic *Cyanobacteria* inhabited the superficial layer while the anoxic phototrophs dominated underneath (Konhauser 2007; Liu et al., 2011; Coman et al., 2013; Pagaling et al. 2012; Hanada, 2016). The occurrence of these different phototrophic bacteria in superficial and sub-superficial layers could explain the various color observed in the sampled encrustations.

The occurrence of various cyanobacterial OTUs were likely linked to water temperature. It has previously been documented that *Fischerella* species prevails at temperatures around 40 °C (Konhauser 2007) corresponding to C4 site, while *Leptolyngbya* prefers temperatures around 55 °C (McGregor and Rasmussen 2008; Roeselers et al. 2007; Sompong et al. 2008) corresponding to C1 site. The high occurrence of filamentous *Cyanobacteria*, such as *Leptolyngbya* and *Spirulina*, is a typical feature of most hot springs worldwide (Amarouche-Yala et al., 2014; Subudhi et al., 2018; Valeriani et al., 2018; Della Porta et al., 2021).

Due to the different oxygen availability, anoxygenic phototrophic microorganisms dominated the sub-superficial layer and were mainly represented by green and purple sulfur/non-sulfur bacteria, such as members of *Chlorobi*, *Chloroflexi* and *Alphaproteobacteria*. Green sulfur bacteria, mainly affiliated with family *Chlorobiaceae*, were found in biofilm along the channel in line with their

602 anaerobic and autotrophic metabolism (Imhoff, 2014). These phototrophs are able to oxidize
603 elemental sulfur and sulfide and to carry out photosynthesis only under anoxic conditions (Asao and
604 Madigan 2010; Imhoff 2014; Madigan et al., 2017). Furthermore, the occurrence of *Chloroflexi*,
605 affiliated with family *Anaerolinaceae* or genus *Roseiflexus*, currently known as "Filamentous
606 Anoxygenic Phototrophs", was previously reported in thermophilic cyanobacterial mats (Gaisin et
607 al., 2016; Kambura et al., 2016; Tank et al., 2017; Valeriani et al., 2018).
608 Anaerobic and anoxygenic phototrophic purple non sulfur bacteria were frequently reported in
609 sulfidic hot springs with temperature around 50 °C (Ainon, Tan and Vikineswary, 2006; Bilyj et al.,
610 2014; Imhoff, 2017). In line with this finding, members of *Alphaproteobacteria*, mainly affiliated
611 with *Rhodomicrobium* genus, were encountered in biofilm samples along the channel. Members of
612 this genus preferably grow photoheterotrophically under anoxic conditions in the light, but they can
613 also use hydrogen, sulfide or ferrous iron as electrons sources (Imhoff et al., 2005).
614

615 **5.3 Evidences from mineralogical analyses and theoretical computations**

616 Mineralogical investigations assessed the widespread presence of calcite throughout the *PC* channel,
617 as also evidenced by the numerical model for which calcite precipitation was driven by CO_2 degassing
618 from the *PC* supersaturated water. Nevertheless, calcite was detected in two distinct morphologies,
619 indicating the occurrence of different precipitation processes. Euhedral calcite can be ascribed to a
620 purely inorganic precipitation process, as expected from the theoretical computations, whereas shrub
621 precipitates are related to the interaction with microbial communities and biofilms (e.g. Allen et al,
622 2000 and reference therein). This latter morphology was found in association with inorganic calcite,
623 irrespectively of the color of the sampled encrustations and of the microbial community composition.
624 Despite the occurrence of diverse cyanobacterial OTUs at increasing distance from the hot spring as
625 a function of water temperature, calcite shrubs were constantly present along the whole channel.
626 Accordingly, both empirical and theoretical observations excluded a biologically controlled or
627 induced precipitation of calcite shrub deposits, which were to be ascribed to abiotic processes.

However, whilst no evidence was found to indicate an active role by microbial metabolism in calcite precipitation, the shrub fabric might be influenced by the presence of microbial mats through organomineralization (e.g. Perry et al., 2007; Dupraz et al., 2009; Allen et al., 2000; Bastianini et al. 2019).This mineral precipitation typically occurs in supersaturated waters by nucleation on bacterially produced polymers, such as those composing cell walls or extracellular polymeric substances (EPS). EPS can indeed account for over 90% of biofilm dry mass (Flemming and Wingender, 2010), forming the scaffold for the biofilm architecture and internal cohesion and allowing adhesion to surfaces. Accordingly, *Cyanobacteria*, which are among the main contributors to the production of EPS in microbial mats (e.g. Rossi and De Philippis, 2015), dominated the microbial community inhabiting the surficial layer of the biofilm along the *PC* channel. Even though calcite precipitation did not seem to be related to microbial activity, the cyanobacterial and prokaryotic colonization along the *PC* channel occurred simultaneously with the formation of calcite nucleation. In fact, the mutual relationship between *Spirulina*-like cells, *Bacteria* and other prokaryotic cells was evident with the tridimensional structure examination of biofilm grown on microscopy slides on the central point of the *PC* channel (**Fig. 6**). This finding is paralleled with the evolution of the crystal weathering traced by the SEM investigation of the calcite precipitates as a function of time (**Fig. 9**). These evidences agree with those reported by a recent study on active travertine deposits from Central Italy (Della Porta et al., 2021), including the Viterbo thermal area, and with previous observations on the *PC* channel (Di Benedetto et al., 2011), which ascribed the structural anomaly of calcite precipitates to the presence of organic polymers embedded in the growing crystals. Accordingly, the analysis of the lattice strain showed structural features similar to those previously described for this site and attributed to bio-mineralized calcite (Di Benedetto et al., 2011).

Inorganic and shrub calcite precipitates exhibited evidence of two distinct redissolution processes. The first one provided progressive consumption of crystals from the edges and/or some existing pits (**Fig. 7c**), indicating a balance between crystal growth and redissolution process. The second process

consisted of a specific pitting, starting from either crystal defects or centers of well-formed crystalline surfaces, to produce evident circular pits (**Fig. 7d**). These features are commonly associated with microbial mats containing sulfur-oxidizing bacteria (Leprich et al., 2021) and ascribed to acidity buffering generated during sulfur oxidation at the microscale through calcite weathering (e.g. Dupraz et al., 2009; Yang et al., 2019). Accordingly, the observed circular pitting was likely the result of the metabolic activity of the S-oxidizing bacteria recognized in the water column (i.e., *Thiofaba*, *Epsilonproteobacteria*) and microbial mats (i.e., *Chlorobi*, *Chloroflexi*). The temporal evolution investigated by the glass slides inserted in the water flow of the channel allowed to give a rough estimation of the time necessary to the precipitate-biofilm system to attain a stable configuration. In particular, we observed that this dynamical equilibrium was reached in about 3 weeks.

Differently from calcite, the numerical model revealed that the *PC* waters were undersaturated with respect to gypsum. Nevertheless, the occurrence of this mineral phase was widely detected along the channel, though in very localized assemblages. The morphological observations on the retrieved crystals indicated that gypsum sporadically nucleated and grew very fast. These evidences allowed to speculate that the observed gypsum crystals were the result of a biologically-induced mineralization, where microbial activity modified the local microenvironment creating favorable conditions for chemical precipitation, as previously observed in other hydrothermal aquatic systems (Tang et al., 2014). It can be hypothesized that S-oxidizing bacteria produced a local anomaly in sulfate concentration inducing local supersaturated conditions and, thus, gypsum precipitation in fractal clusters of crystals. This hypothesis could be supported by the presence of several sulfur-oxidizing bacteria (e.g. *Thiofaba*, *Chloroflexi* and *Chlorobi*) along the *PC* channel in both the water column and biofilm layers. A similar mechanism was previously proposed for both *Bacteria* (Thompson and Ferris, 1990; Canfora et al., 2016) and microfungi (Cecchi et al., 2018). Notably, contrary to what expected from the physicochemical conditions characterizing the *PC* channel, no evidences of dissolution processes were observed for gypsum. It appeared to be preserved from dissolution when embedded in the biofilm, pointing to a critical role of microbial mats in governing

680 the mobility of chemical species at the water-travertine interface. These evidences were in line with
681 the findings by Canfora et al. (2016) according to which cyanobacteria would be capable to promote,
682 either directly or indirectly, the formation of a protective envelope made of carbonates and/or sulfates.
683

684 **6. Conclusions**

685 In the *PC* system, a sharp temperature gradient along the channel was associated with a chemical
686 evolution of the water and dissolved gas composition. The latter was mainly driven by inorganic
687 processes (water-atmosphere exchange), resulting in active travertine deposition. Travertine
688 encrustations were characterized by the presence of microbial mats with a well-stratified microbial
689 community, mainly shaped by light availability, which influenced the morphology of the mineral
690 phases with euhedral calcite crystals (inorganically produced by CO_2 degassing) coexisting with
691 calcite shrub (likely ascribed to organomineralization). Despite the geochemical modelling based on
692 measured ion concentrations indicated undersaturation conditions with respect to gypsum,
693 mineralogical analyses revealed the occurrence of this mineral embedded in the biofilm. This
694 apparent contradiction between physicochemical environmental conditions and mineralogical
695 evidences can be reconciled by hypothesizing the establishment of chemical gradients at the
696 microscale triggered by bacterial activity. In particular, the chemolithoheterotrophic oxidation of
697 reduced sulfur operated by microbial consortia was expected to produce a local increase in sulfate
698 concentration, determining supersaturated microenvironmental conditions that promoted
699 precipitation of gypsum crystals. This hypothesis was sustained by the recognition of circular pitting
700 on calcite crystals related to dissolution processes induced by the metabolic activity of sulfur-
701 oxidizing bacteria. On the other hand, microbial mats may exert a protective functioning with respect
702 to gypsum crystals, preventing dissolution despite the overall undersaturation conditions of the *PC*
703 channel, suggesting the capability of microbial mats in modulating environmental mobility of
704 chemical species.

Acknowledgments

CNR-IRSA participation was supported by Fondazione CARIPLO contract No. 2014-1301 (BATA Project). Maria Rosa Siena e Giulia Giagnoli (CNR-IRSA) are gratefully acknowledged for the help in sampling and CARD-FISH analysis. Laura Chiarantini, Mario Paolieri and Laura Chelazzi are gratefully acknowledged for their unvaluable help in the SEM and XRD investigation, respectively. The MEMA (Microscopy and Microanalysis) and the CRIST (Structural Crystallography) Interdepartmental Centers of the University of Florence are acknowledged for provision of experimental access at their facilities. FDB acknowledges University of Florence, for granting him under the Progetto di Ateneo funds, and the University of Ferrara, for granting him under the FAR2021 and FAR2022 funds. Financial support by the Laboratory of Fluid Geochemistry of the Department of Earth Sciences (University of Florence) is also acknowledged.

719 **References**

720 Airnon H., Tan C.J., Vikineswary S., 2006. Biological Characterization of *Rhodomicrobium vannielii* Isolated
721 from a Hot Spring at Gadek, Malacca, Malaysia. Malaysian Journal of Microbiology 2, 15-21; doi:
722 10.21161/mjm.210603.s.

723 Albertsen M., Karst S.M., Ziegler A.S., Kirkegaard R.H., Nielsen, P.H., 2015. Back to Basics – The Influence
724 of DNA Extraction and Primer Choice on Phylogenetic Analysis of Activated Sludge Communities.
725 PLoS One 10, e0132783; doi: 10.1371/journal.pone.0132783.

726 Allen C.C., Albert F.G., Chafetz H.S., Combie J., Graham C.R., Kieft T.L., Kivett S.J., McKay D.S., Steele
727 A., Taunton A.E., Taylor M.R., Thomas-Keprta K.L., Westall F., 2000. Microscopic physical
728 biomarkers in carbonate hot springs: implications in the search for life on Mars. Icarus 147, 49-67;
729 doi: 10.1006/icar.2000.6435.

730 Amalfitano S., Fazi S., 2008. Recovery and quantification of bacterial cells associated with streambed
731 sediments. Journal of Microbiological Methods 75, 237–243; doi: 10.1016/j.mimet.2008.06.004.

732 Amalfitano S., Del Bon A., Zoppini A., Ghergo S., Fazi S., Parrone D., Casella P., Stano F., Preziosi E., 2014.
733 Groundwater geochemistry and microbial community structure in the aquifer transition from volcanic
734 to alluvial areas. Water Research 65, 384-394; doi: 10.1016/j.watres.2014.08.004.

735 Amarouche-Yala S., Benouadah A., El Ouahab Bentabet A., López-García P., 2014. Morphological and
736 phylogenetic diversity of thermophilic cyanobacteria in Algerian hot springs. Extremophiles 18, 1035-
737 1047; doi: 10.1007/s00792-014-0680-7.

738 Asao, M., Madigan, M.T., 2010. Taxonomy, phylogeny, and ecology of the heliobacteria. Photosynthesis
739 Research 104, 103-111; doi: 10.1007/s11120-009-9516-1.

740 Banfield J.F., Moreau J.W., Chan C.S., Welch A., Little B., 2021. Mineralogical biosignatures and the search
741 for life on Mars. Astrobiology 1, 447-465; doi: 10.1089/153110701753593856.

742 Bastianini L., Rogerson M., Mercedes-Martín R., Prior T.J., Cesar E.A., Mayes W.M., 2019. What Causes
743 Carbonates to Form “Shrubby” Morphologies? An Anthropocene Limestone Case Study. Frontiers in
744 Earth Science 7:236; doi: 10.3389/feart.2019.00236.

745 Bilyj M., Lepitzki D., Hughes E., Swiderski J., Stackebrandt E., Pacas C., Yurkov V. V, 2014. Abundance and
746 Diversity of the Phototrophic Microbial Mat Communities of Sulphur Mountain Banff Springs and
747 Their Significance to the Endangered Snail, *Physella johnsoni*. Open Journal of Ecology 4, 488-516.

748 Bolger A.M., Lohse M., and Usadel B., 2014. Trimmomatic: A flexible trimmer for Illumina sequence data.
749 Bioinformatics 30, 2114-2120; doi: 10.1093/bioinformatics/btu170.

750 Cadogan S.P., Maitland G.C., Trusler P.M., 2014. Diffusion coefficients of CO_2 and N_2 in water at
751 temperatures between 298.15 K and 423.15 K at pressures up to 45 MPa. Journal of Chemical &
752 Engineering Data 59, 519-525.

753 Campbell B.J., Engel A.S., Porter M.L., Takai K., 2006. The versatile ε-proteobacteria: Key players in
754 sulphidic habitats. Nature Reviews Microbiology 4, 458-468; doi: 10.1038/nrmicro1414.

755 Canfora L., Vendramin E., Vittori Antisari L., Lo Papa G., Dazzi C., Benedetti A., Iavazzo P., Adamo P.,
756 Jungblut A., Pinzari F., 2016. Compartmentalization of gypsum and halite associate with
757 cyanobacteria in saline soil crusts. FEMS Microbiology Ecology 92, fiw080; doi:
758 10.1093/femsec/fiw080.

759 Caporaso J.G., Kuczynski J., Stombaugh J., Bittinger K., Bushman F.D., Costello E.K., Fiere N., Gonzalez
760 Peña A., Goodrich J.K., Gordon J.I., Huttley G.A., Kelley S.T., Knights D., Koenig J.E., Ley R.E.,
761 Lozupone C.A., McDonald D., Muegge B.D., Pirrung M., Reeder J., Sevinsky J.R., Turnbaugh P.J.,
762 Walters W.A., Widmann J., Yatsunenko T., Zaneveld J., Knight R., 2010. QIIME allows analysis of
763 high-throughput community sequencing data. Nature Methods 7, 335-336; doi: 10.1038/nmeth.f.303.

764 Caporaso J.G., Lauber C.L., Walters W.A., Berg-Lyons D., Huntley J., Fierer N., Owens S.M., Betley J., Fraser
765 L., Bauer M., Gormley N., Gilbert J.A., Smith G., Knight R., 2012. Ultra-highthroughput microbial
766 community analysis on the Illumina HiSeq and MiSeq platforms. The ISME journal 6, 1621-1624;
767 doi: 10.1038/ismej.2012.8.

768 Casentini B., Falcione F.T., Amalfitano S., Fazi S., Rossetti S., 2016. Arsenic removal by discontinuous ZVI
769 two steps system for drinking water production at household scale. Water Research 106, 135-145.

770 Castro-Alonso M.J., Montañez-Hernandez L.E., Sanchez-Muñoz M.A., Franco M.R.M., Narayanasamy R.,
771 Balagurusamy N., 2016. Microbially induced calcium carbonate precipitation (MICP) and its potential
772 in bioconcrete: microbiological and molecular concepts. Frontiers in Materials 6:126; doi:
773 10.3389/fmats.2019.00126.

774 Cecchi G., Marescotti P., Di Piazza S., Lucchetti G., Mariotti M.G., Zotti M., 2018. Gypsum biomineralization
775 in sulphide-rich hardpans by a native *Trichoderma harzianum* Rifai strain. Geomicrobiology Journal
776 35, 209-214; doi: 10.1080/01490451.2017.1362077.

777 Chiriac C.M., Szekeres E., Rudi K., Baricz A., Hegedus A., Dragoş N., Coman C., 2017. Differences in
778 temperature and water chemistry shape distinct diversity patterns in thermophilic microbial
779 communities. Applied and Environmental Microbiology 83, e01363-17; doi: 10.1128/AEM.01363-17.

780 Cinti D., Tassi F., Procesi M., Bonini M., Capecchiacci F., Voltattorni N., Vaselli O., Quattrocchi F., 2014.
781 Fluid geochemistry and geothermometry in the unexploited geothermal field of the Vicano–Cimino
782 Volcanic District (Central Italy). Chemical Geology 371, 96-114.

783 Coman C., Druga B., Hegedus A., Sicora C., Dragoş N., 2013. Archaeal and bacterial diversity in two hot
784 spring microbial mats from a geothermal region in Romania. Extremophiles 17, 523-534; doi:
785 10.1007/s00792-013-0537-5.

786 Corey A. T., 1954. The interrelation between gas and oil relative permeabilities. *Prod. Mon.* 19, 38-41.

787 Della Porta G., Hoppert M., Hallmann C., Schneider D., Reitner J., 2021. The influence of microbial mats on
788 travertine precipitation in active hydrothermal systems (Central Italy). The Depositional Record 00, 1-
789 45; doi: 10.1002/dep2.147.

790 Des Marais D.J., Walter M.R., 2019. Terrestrial hot spring systems: Introduction. Astrobiology 19, 1419-1432;
791 doi: 10.1089/ast.2018.19761419.

792 Di Benedetto F., Montegrossi G., Minissale A., Pardi L.A., Romanelli M., Tassi F., Delgado Huertas A.,
793 Pampin E.M., Vaselli O., Borrini D., 2011. Biotic and inorganic control on travertine deposition at
794 Bullicame 3 spring (Viterbo, Italy): A multidisciplinary approach. Geochimica et Cosmochimica Acta
795 75, 4441-4455; doi :10.1016/j.gca.2011.05.011.

796 Duchi V., Minissale A., Romani L., 1985. Studio geochimico su acque e gas dell'area geotermica lago di Vico-
797 M.Cimini (Viterbo). Atti della Societa Toscana di Scienze Naturali Residente in Pisa, Memorie,
798 Processi Verbali, Serie A 92, 237-254.

799 Duchi V., Minissale A., 1995. Distribuzione delle manifestazioni gassose nel settore peritirrenico Tosco–
800 Laziale e loro interazione con gli acquiferi superficiali. Boll. Soc. Geol. Ital. 114, 337-351.

801 Dupraz C., Reid R.P., Braissant O., Decho A.W., Norman R.S., Visscher P.T., 2009. Processes of carbonate
802 precipitation in modern microbial mats. Earth-Science Reviews 96, 141-162; doi:
803 10.1016/j.earscirev.2008.10.005.

804 Evans W. C., White L. D., Rapp J. B., 1988. Geochemistry of some gases in hydrothermal fluids from the
805 southern Juan de Fuca Ridge. Journal of Geophysical Research 93(B12), 15305-15313.

806 Fazi S., Amalfitano S., Pizzetti I., Pernthaler J., 2007. Efficiency of fluorescence in situ hybridization for
807 bacterial cell identification in temporary river sediments with contrasting water content. Systematic
808 and Applied Microbiology 30, 463-470; doi: 10.1016/j.syapm.2007.03.003.

809 Fazi S., Vázquez E., Casamayor E.O., Amalfitano S., Butturini A., 2013. Stream Hydrological Fragmentation
810 Drives Bacterioplankton Community Composition. PLoS One 8, e64109; doi:
811 10.1371/journal.pone.0064109.

812 Flemming H.C., Wingender J., 2010. The biofilm matrix. Nature Reviews 8, 623-633.

813 Gaisin V.A., Grounzdev D.S., Namsaraev Z.B., Sukhacheva M.V., Gorlenko V.M., Kuznetsov B.B., 2016.
814 Biogeography of thermophilic phototrophic bacteria belonging to Roseiflexus genus, FEMS
815 Microbiology Ecology 92, fiw012; doi: 10.1093/femsec/fiw012.

816 Giampaoli S., Valeriani F., Gianfranceschi G., Vitali M., Delfini M., Festa M.R., Bottari E., Romano Spica
817 V., 2013. Hydrogen sulfide in thermal spring waters and its action on bacteria of human origin.
818 Microchemical Journal 108, 210-214; doi: 10.1016/j.microc.2012.10.022.

819 Görgen S., Benzerara K., Skouri-Panet F., Gugger M., Chauvat F., Cassier-Chauvat C., 2020. The diversity of
820 molecular mechanisms of carbonate biomineralization by bacteria. Discover Materials 1, 2; doi:
821 10.1007/s43939-020-00001-9.

822 Graf D.L., 1961. Crystallographic tables for the rhombohedral carbonates. American Mineralogist 46, 1283-
823 1316.

824 Greuter D., Loy A., Horn M., Rattei T., 2016. ProbeBase-an online resource for rRNA-targeted oligonucleotide
825 probes and primers: New features 2016. Nucleic Acids Research 44, D586-D589; doi:
826 10.1093/nar/gkv1232.

827 Gulecal-Pektas Y., Temel M., 2017. A Window to the Subsurface: Microbial Diversity in Hot Springs of a
828 Sulfidic Cave (Kaklik, Turkey). Geomicrobiology Journal 34, 374-384; doi:
829 10.1080/01490451.2016.1204374.

830 Gumerov V.M., Mardanov A. V, Beletsky A. V, Osmolovskaya E.A.B., Ravin N. V, 2011. Molecular Analysis
831 of Microbial Diversity in the Zavarzin Spring, Uzon Caldera, Kamchatka. Microbiology 80, 244-251;
832 doi: 10.1134/S002626171102007X.

833 Hanada S., 2016. Anoxygenic Photosynthesis — A Photochemical Reaction That Does Not Contribute to
834 Oxygen Reproduction —. Microbes and Environments 31, 1-3; doi:10.1264/jsme2.ME3101rh.

835 Huang Q., Dong C.Z., Dong R.M., Jiang H., Wang S., Wang G., Fang B., Ding X., Niu L., Li X., 2011.
836 Archaeal and bacterial diversity in hot springs on the Tibetan Plateau, China. Extremophiles 15, 549-
837 563; doi: 10.1007/s00792-011-0386-z.

838 Illumina I., 2015. 16S Metagenomic Sequencing Library Preparation, Part # 15044223 Rev. B. Illumina, San
839 Diego, CA.
840 https://support.illumina.com/documents/documentation/chemistry_documentation/16s/16s-
841 metagenomic-library-prep-guide-15044223-b.pdf

842 Imhoff J.F., 2005. Genus XVI. Rhodomicrobium. In: Brenner, D.J., Krieg, N.R. and Staley, J.T., Eds.,
843 Bergey's Manual of Systematic and Determinative Bacteriology, Springer, New York, 543-454.

844 Imhoff J.F., 2014. Biology of green sulfur bacteria. eLS John Wiley & Sons Ltd, Chichester;
845 doi:10.1002/9780470015902.a0000458.pub2.

846 Kambura A.K., Mwirichia R.K., Kasili R.W., Karanja E.N., Makonde H.M., Boga H.I., 2016. Bacteria and
847 Archaea diversity within the hot springs of Lake Magadi and Little Magadi in Kenya. BMC
848 Microbiology 16, 1-12; doi: 10.1186/s12866-016-0748-x.

849 Kemp P., Aller J., 2004. Bacterial diversity in aquatic and other environments: what 16S rDNA libraries can
850 tell us. FEMS Microbiology Ecology 47, 161-177; doi: 10.1016/S0168-6496(03)00257-5.

851 Konhauser K., 2007. Introduction to Geomicrobiology, Blackwell Publishing, Oxford.

852 Lebaron P., Servais P., Agogue H., Courties C., Joux F., 2001. Does the high nucleic acid content of individual
853 bacterial cells allow us to discriminate between active cells and inactive cells in aquatic systems?
854 Applied and Environmental Microbiology 67, 1775-1782; doi: 10.1128/AEM.67.4.1775-1782.2001.

855 Leprich D.J., Flood B.E., Schroedl P.R., Ricci E., Marlow J.J., Girguis P.R., Bailey J.V., 2021. Sulfur bacteria
856 promote dissolution of authigenic carbonates at marine methane seeps. The ISME Journal 15, 2043-
857 2056; doi: 10.1038/s41396-021-00903-3.

858 Liu Z., Klatt C.G., Wood J.M., Rusch D.B., Ludwig M., Wittekindt N., Tomsho L.P., Schuster S.C., Ward
859 D.M., Bryant D.A., 2011. Metatranscriptomic analyses of chlorophototrophs of a hot-spring microbial
860 mat. The ISME Journal 5, 1279-1290; doi: 10.1038/ismej.2011.37.

861 Lupini G., Proia L., Di Maio M., Amalfitano S., Fazi S., 2011. CARD-FISH and confocal laser scanner
862 microscopy to assess successional changes of the bacterial community in freshwater biofilms. Journal
863 of Microbiological Methods 86, 248-251; doi:10.1016/j.mimet.2011.05.011.

864 Madigan M.T., Schaaf N.A.V., Sattley W.M.., 2017. The Chlorobiaceae, Chloroflexaceae, and
865 Heliobacteriaceae. In: Hallenbeck P. (eds) Modern Topics in the Phototrophic Prokaryotes. Springer,
866 Cham; doi: 10.1007/978-3-319-46261-5_4.

McGregor G.B., Rasmussen J.P., 2008. Cyanobacterial composition of microbial mats from an Australian thermal spring: a polyphasic evaluation. FEMS Microbiology Ecology 63, 23–35; doi: 10.1111/j.1574-6941.2007.00405.x.

McIlroy S.J., Saunders A.M., Albertsen M., Nierychlo M., McIlroy B., Hansen A.A., Karst S.M., Nielsen J.L., Nielsen P.H., 2015. MiDAS: the field guide to the microbes of activated sludge. Database 2015, bav062; doi: 10.1093/database/bav062.

Minissale A., Kerrick D. M., Magro G., Murrell M. T., Paladini M., Rihs S., Sturchio N.C., Tassi F., Vaselli O., 2002. Geochemistry of quaternary travertines in the region north of Rome (Italy): Structural, hydrologic and paleoclimatic implications. Earth and Planetary Science Letters 203, 709-728; doi: 10.1016/S0012-821X(02)00875-0.

Minissale A., 2004. Origin, transport and discharge of CO_2 in Central Italy. Earth-Science Reviews 66, 89-141; doi: 10.1016/j.earscirev.2003.09.001.

Mori K., Suzuki K., 2008. *Thiofaba tepidiphila* gen. nov., sp. nov., a novel obligately chemolithoautotrophic, sulfur-oxidizing bacterium of the *Gammaproteobacteria* isolated from a hot spring. International Journal of Systematic and Evolutionary Microbiology 58, 1885-1891; doi: 10.1099/ijs.0.65754-0.

Pagaling E., Grant W.D., Cowan D.A., Jones B.E., Ma Y., Ventosa A., Heaphy, 2012. Bacterial and archaeal diversity in two hot spring microbial mats from the geothermal region of Tengchong, China. Extremophiles 16, 607-618; doi: 10.1007/s00792-012-0460-1.

Palandri J.L., Kharaka Y.K., 2004. A compilation of rate parameters of water-mineral interaction kinetics for application to geochemical modeling. USGS Open File Report 2004-1068, Menlo Park, California, National Energy Technology Laboratory – United States Department of Energy, 64 pp.

Pentecost A., 1995. Geochemistry of carbon dioxide in six travertine-depositing waters of Italy. Journal of Hydrology 167, 263-278.

Perry R.S., Mcloughlin N., Lynne B.Y., Sephton M.A., Oliver J.D., Perry C.C., Campbell K., Engel M.H., Farmer J.D., Brasier M.D., Staley J.T., 2007. Defining biominerals and organominerals: direct and indirect indicators of life. Sedimentary Geology 201, 157-179; doi: 10.1016/j.sedgeo.2007.05.014.

893 Piscopo V., Barbieri M., Monetti V., Pagano G., Pistoni S., Ruggi E., Stanzione D., 2006. Hydrogeology of
894 thermal waters in Viterbo area, central Italy. Hydrogeology Journal 14, 1508-1521; doi:
895 10.1007/s10040-006-0090-8.

896 Portillo M.C., Sririn V., Kanoksilapatham W., Gonzalez J.M., 2009. Differential microbial communities in hot
897 spring mats from Western Thailand. Extremophiles 13, 321-331; doi: 10.1007/s00792-008-0219-x.

898 Prieto-Barajas C.M., Valencia-Cantero E., Santoyo G., 2018. Microbial mat ecosystems: Structure types,
899 functional diversity, and biotechnological application. Electronic Journal of Biotechnology 31, 48-56;
900 doi: 10.1016/j.ejbt.2017.11.001.

901 Pruess K., Oldenburg C., Moridis G., 2012. TOUGH2 USER'S GUIDE, VERSION 2. LBNL-43134.

902 Rimondi V., Costagliola P., Lattanzi P., Catelani T., Fornasaro S., Medas D., Morelli G., Paolieri M., 2021.
903 Bioaccesible arsenic in soil of thermal areas of Viterbo, Central Italy: implications for human health
904 risk. Environmental Geochemistry and Health; doi: 10.1007/s10653-021-00914-1.

905 Rodriguez-Carvajal J., 1993. Recent advances in magnetic structure determination by neutron powder
906 diffraction. Physica B: Condensed Matter 192, 55-69; doi: 10.1016/0921-4526(93)90108-I.

907 Roeselers G., Norris T.B., Castenholz R.W., Rysgaard S., Glud R.N., Kühl M., Muyzer G., 2007. Diversity of
908 phototrophic bacteria in microbial mats from Arctic hot springs (Greenland). Environmental
909 Microbiology 9, 26-38; doi: 10.1111/j.1462-2920.2006.01103.x.

910 Rossi F., De Philippis R., 2015. Role of cyanobacterial exopolysaccharides in phototrophic biofilms and in
911 complex microbial mats. Life 5, 1218-1238; doi: 10.3390/life5021218.

912 Salata G.G., Roelke L.A., Cifuentes L.A., 2000. A rapid and precise method for measuring stable carbon
913 isotope ratios of dissolved inorganic carbon. Marine Chemistry 69, 153-161.

914 Schuler C.G., Having J.R., Hamilton T.L., 2017. Hot spring microbial community composition, morphology,
915 and carbon fixation: implications for interpreting the ancient rock record. Frontiers in Earth Science
916 5: 97; doi: 10.3389/feart.2017.00097.

Sompong U., Anuntalabhochai S., Cutler R.W., Castenholz R.W., Peerapornpisal Y., 2008. Morphological and phylogenetic diversity of cyanobacterial populations in six hot springs of Thailand. Science Asia 34, 153-162; doi: 10.2306/scienceasia1513-1874.2008.34.153.

Stal L.J., Bolhuis H., Cretoiu M.S., 2017. Phototrophic Microbial Mats. In: Hallenbeck P. (eds) Modern Topics in the Phototrophic Prokaryotes. Springer, Cham; doi: 10.1007/978-3-319-46261-5_9.

Subudhi E., Sahoo R.K., Gaur M., Singh A., Das A., 2018. Shift in Cyanobacteria Community Diversity in Hot Springs of India. Geomicrobiology Journal 35, 141-147; doi: 10.1080/01490451.2017.1338799.

Sundberg C., Al-Soud W.A., Larsson M., Alm E., Shakeri Yekta S., Svensson B.H., Sørensen S.J., Karlsson A., 2013. 454-Pyrosequencing Analyses of Bacterial And Archaeal Richness In 21 Full-Scale Biogas Digesters. FEMS Microbiology Ecology 85, 612-626; doi: 10.1111/1574-6941.12148.

Tang M., Ehreiser A., Li Y.L., 2014. Gypsum in modern Kamchatka volcanic hot springs and the Lower Cambrian black shale: applied to the microbial-mediated precipitation of sulfates on Mars. American Mineralogist 99,2126-2137; doi: 10.2138/am-2014-4754.

Tank M., Thiel V., Ward D.M., Bryant D.A., 2017. A Panoply of Phototrophs: An Overview of the Thermophilic Chlorophototrophs of the Microbial Mats of Alkaline Siliceous Hot Springs in Yellowstone National Park, WY, USA. In: Hallenbeck P. (eds) Modern Topics in the Phototrophic Prokaryotes. Springer, Cham; doi: 10.1007/978-3-319-46261-5_3.

Tassi F., Vaselli O., Luchetti G., Montegrossi G., Minissale A., 2008. Metodo per la determinazione dei gas disciolti in acque naturali. Int. Rep., CNR-IGG, Florence, Italy, pp. 11.

Tassi F., Vaselli O., Tedesco D., Montegrossi G., Darrah T., Cuoco E., Mapendano M.Y., Poreda R., Delgado Huertas A., 2009. Water and gas chemistry at Lake Kivu (DRC): geochemical evidence of vertical and horizontal heterogeneities in a multi-basin structure. Geochemistry Geophysics Geosystems 10(2). http://dx.doi. org/10.1029/2008GC002191.

Tassi F., Venturi S., Cabassi J., Vaselli O., Gelli I., Cinti D., Capecchiacci F., 2015. Biodegradation of CO_2, CH_4 and volatile organic compounds (VOCs) in soil gas from the Vicano-Cimino hydrothermal system (central Italy). Organic Geochemistry 86, 81-93; doi: 10.1016/j.orggeochem.2015.06.004.

943 Tassi F., Fazi S., Rossetti S., Pratesi P., Ceccotti M., Cabassi J., Capecchiacci F., Venturi S., Vaselli O., 2018.
944 The biogeochemical vertical structure renders a meromictic volcanic lake a trap for geogenic CO_2
945 (Lake Averno, Italy). PLoS ONE 13(3): e0193914; doi: 10.1371/journal.pone.0193914.

946 Thompson J.B., Ferris F.G., 1990. Cyanobacterial precipitation of gypsum, calcite, and magnesite from natural
947 alkaline lake water. Geology 18, 995-998.

948 Valeriani F., Crognale S., Protano C., Gianfranceschi G., Orsini M., Vitali M., Spica V.R., 2018. Metagenomic
949 analysis of bacterial community in a travertine depositing hot spring. New Microbiologica 41, 126-
950 135.

951 Van Gemerden H., 1993. Microbial mats: A joint venture. Marine Geology 113, 3-25.

952 Van Driessche A.E.S., Stawski T.M., Kellermeier M., 2019. Calcium sulfate precipitation pathways in natural
953 and engineered environments. Chemical Geology 530, 119274; doi: 10.1016/j.chemgeo.2019.119274.

954 Vaselli O., Tassi F., Montegrossi G., Capaccioni B., Giannini L., 2006. Sampling and analysis of volcanic
955 gases. Acta Vulcanologica 18, 65-76.

956 Venturi S., Tassi F., Bicocchi G., Cabassi J., Capecchiacci F., Capasso G., Vaselli O., Ricci A., Grassa F.,
957 2017. Fractionation processes affecting the stable carbon isotope signature of thermal waters from
958 hydrothermal/volcanic systems: The examples of Campi Flegrei and Volcano Island (southern Italy).
959 Journal of Volcanology and Geothermal Research 345, 46-57; doi: 10.1016/j.jvolgeores.2017.08.001.

960 Wang Q., Garrity G.M., Tiedje J.M., Cole J.R., 2007. Naive Bayesian classifier for rapid assignment of rRNA
961 sequences into the new bacterial taxonomy. Applied and Environmental Microbiology 73, 5261-5267;
962 doi: 10.1128/AEM.00062-07.

963 Wang S., Hou W., Dong H., Jiang H., Huang L., Wu G., Zhang C., Song Z., Zhang Y., Ren H., Zhang J.,
964 Zhang L., 2013. Control of temperature on microbial community structure in hot springs of the Tibetan
965 Plateau. PLoS ONE 8, e62901; doi: 10.1371/journal.pone.0062901.

966 Wilmeth D. T., Johnson H. A., Stamps B. W., Berelson W. M., Stevenson B. S., Nunn H. S., Grim S. L., Dillon
967 M. L., Paradis O., Corsetti F. A., Spear J. R., 2018. Environmental and Biological Influences on

968 Carbonate Precipitation Within Hot Spring Microbial Mats in Little Hot Creek, CA. Frontiers in
969 Microbiology 9, 1464; doi: 10.3389/fmicb.2018.01464.

970 Xu T., Pruess K., 2001. Modeling multiphase nonisothermal fluid flow and reactive geochemical transport in
971 variably saturated fractured rocks: 1. Methodology. American Journal of Science 301, 16-33.

972 Xu T., Sonnenthal E.L., Spycher N., Pruess K., 2006. TOUGHREACT: a simulation program for non-
973 isothermal multiphase reactive geochemical transport in variably saturated geologic media. Computers
974 & Geosciences 32, 145-165.

975 Yang T., Teske A., Ambrose W., Salman-Carvalho V., Bagnell R., Nielsen L.P., 2019. Intracellular calcite
976 and sulfur dynamics of *Achromatium* cells observed in a lab-based enrichment and aerobic incubation
977 experiment. Antonie van Leeuwenhoek 112, 263-274; doi: 10.1007/s10482-018-1153-2.

978 Zhang J., Quay P.D., Wilbur D.O., 1995. Carbon isotope fractionation during gas-water exchange and
979 dissolution of CO_2. Geochimica et Cosmochimica Acta 59(1), 107-114; doi: 10.1016/0016-
980 7037(95)91550-D.

981

982 **Figure captions**

983 **Fig. 1** Location of the study area in central Italy (**a**), few km west of the town of Viterbo (**b**). The
984 Piscine Carletti spring system is shown, together with the sampling sites along the channel (**c**).

985 **Fig. 2** Results of the numerical model of the channel: **(a)** temperature and **(b)** dissolved CO_2. In the
986 inset, the comparison of the considered parameter, evaluated at 1 cm from the bottom of the channel
987 (blue line), with the corresponding experimental measurement (points), listed in Table 1.

988 **Fig. 3** Results of the numerical model of the channel: **(a)** Ca^{2+} and **(b)** HCO_3^-. In the inset, the
989 comparison of the considered parameter, evaluated at 1 cm from the bottom of the channel (blue line),
990 with the corresponding experimental measurement (points), listed in Table 1. **(c)** Volume fraction of
991 precipitated calcite.

992 **Fig. 4 Water: (a)** Abundance of phylogenetic taxa (Archaea and main phyla within Bacteria) and
993 single classes within Proteobacteria (in blue) in the different water sampling points. (**b**) OTUs relative
994 abundance in water samples estimated by NGS. Bacterial taxa accounting for less than 1% of total
995 composition were classified as 'Other bacteria'.

996 **Fig. 5 Biofilm: (a)** Total prokaryotic abundance in superficial and sub-superficial biofilm samples.
997 **(b)** Total abundance of *Cyanobacteria* and single classes within *Proteobacteria* in superficial and
998 sub-superficial biofilm samples. **(c)** OTUs relative abundance in biofilm samples estimated by NGS.
999 Clusters making up less than 1 % of total composition were classified as 'other Bacteria' or 'other
1000 Archaea'.

1001 **Fig. 6** CLSM combined images showing the spatial distribution (X−Y, X−Z, and Y−Z planes) of
1002 Bacteria (green), Cyanobacteria (red) and other prokaryotes (blue) identified by CARD-FISH in
1003 biofilms. The hybridized bacterial cells were excited with the 488 nm line of an Ar laser (excitation)
1004 and observed in the green channel from 500 to 530 nm (emission). Calcite crystals were visualized
1005 by their reflection signal (405 nm line of a diode laser) and appear of gray color.

Fig. 7 Secondary **(a,b)** and Backscattered **(c-f)** electron micrographs of representative regions of the investigated samples: **(a)** C1W (Magnification: 9580X); **(b)** C3G (3410X); **(c)** C2R (1500X); **(d)** C5G (1500X); **(e)** C3R (2760X); **(f)** C2R (500X).

Fig. 8 Secondary **(a,b-e)** and Backscattered **(b)** electron micrographs of representative regions of the investigated samples: **(a)** C3G (Magnification: 1580X); **(b)** C3G (1580X); **(c)** C8G (1610X); **(d)** C8W (851X); **(e)** C7G (3000X).

Fig. 9 Backscattered electron micrographs of two representative regions of travertine precipitated after **(a)** 14 days and **(b)** 21 days over the glass slide. Magnification: 1000X.

Table captions

Table 1 Physicochemical and isotopic (δ^{13}C-TDIC and δ^{13}C-CO_2) features of the water and dissolved gas samples collected along the *PC* channel.